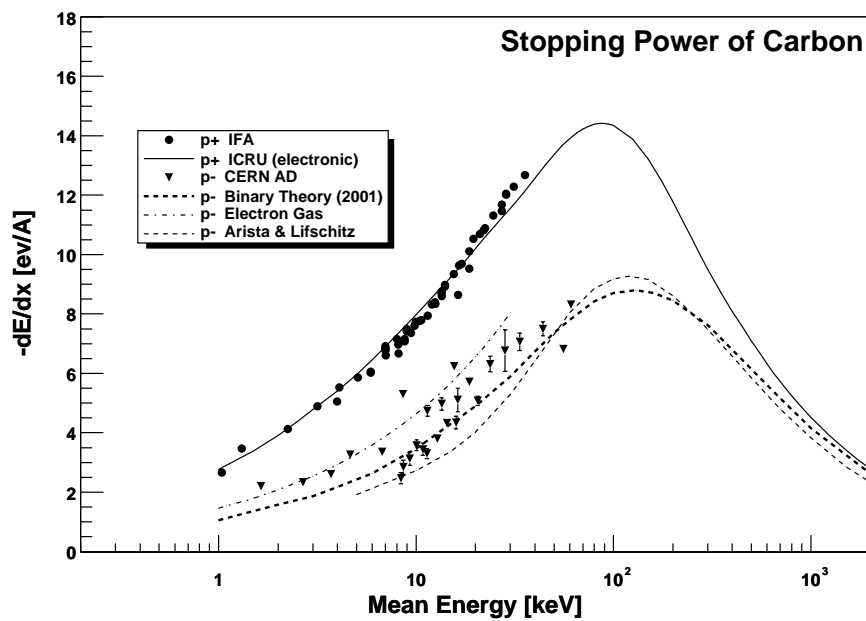# Experimental Investigations of the Energy Loss of Slow Protons and Antiprotons in Matter

Alexandru Csete

Institute of Physics and Astronomy

University of Aarhus

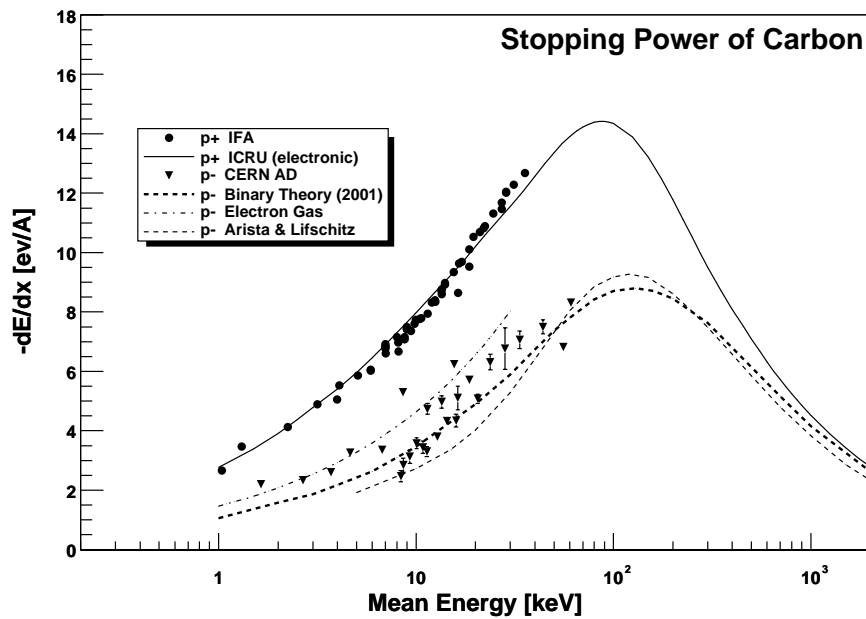M.Sc. Thesis, January 2002

Experimental Investigations of the Energy Loss of Slow Protons and Antiprotons in Matter

Alexandru Csete

Institute of Physics and Astronomy
University of Aarhus

Acknowledgments

Alex

Contents

List of Figures

List of Tables

Chapter 1

Introduction

Penetration of charged particles through matter has been of interest since the very early days of modern atomic physics. One of the pioneers in the study of this phenomenon was Niels Bohr, see e.g. [1], who developed a theoretical framework based mostly on classical mechanics. He was later followed by many others who used both classical and quantum mechanical methods to describe the phenomena connected with this field.

One of the main topics in this context is the energy transfer from the projectiles to the target atoms. Due to the complex nature of atoms many of the existing theoretical models are either too restrictive by making too many assumptions, or use too simple pictures which are not applicable for real physical systems. Furthermore, the fact that the "interesting" range in projectile energy spans over more than eight decades (see figure 1.1) makes things even more complicated. Experimental measurements of the energy loss of particles passing through matter have therefore been playing a very important role in the understanding of these interactions.

When a charged particle traverses matter, it will lose energy due to interaction with the target atoms. The energy loss of the projectile per unit distance in the target material is called the *stopping power* of the material and is usually written as $-\frac{\mathrm{d}E}{\mathrm{d}x}$. It depends on the charge and velocity of the projectile and, of course, the target material. We will exclusively be concerned with protons and antiprotons as projectiles and with energies below the Coulomb barrier of the nucleus, such that nuclear processes do not occur. Under these circumstances, the interaction between the projectile and the target atom is electromagnetic and the energy lost by the penetrating projectile is transfered to the electrons of the target atom. These electrons are either bound to the nucleus or are part of a plasma like in the case of valence electrons. The largest energy transfer occurs when the projectile is in "resonance" with the electrons, that is, if the veloctiy of the projectile is aprroximately the same as the velocity of the target electrons. At higher projectile velocities, the interaction time will be shorter causing reduced momentum transfer ($\Delta \mathbf{p} = \mathbf{F}\Delta t$) corresponding to reduced en-
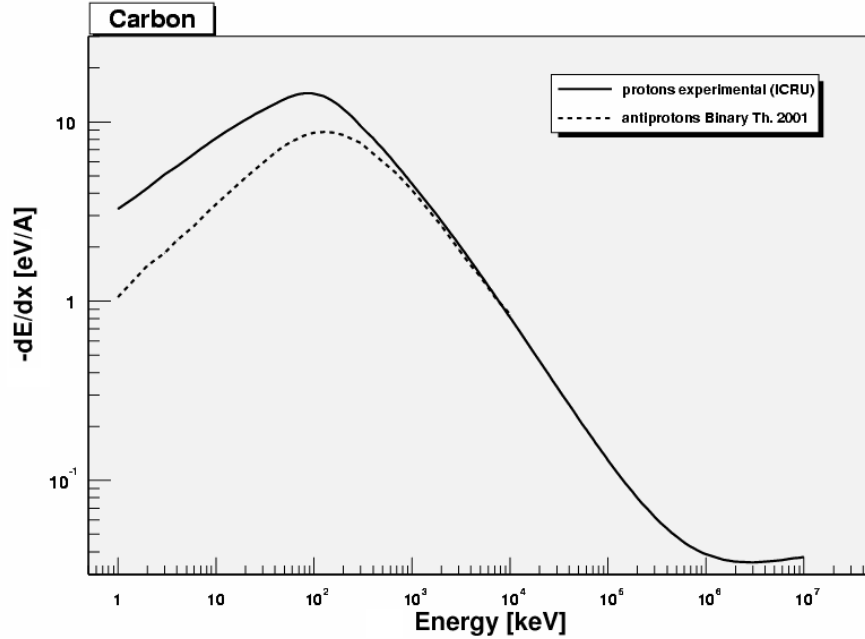
Figure 1.1: The stopping power of amorphous carbon as a function of projectile energy for protons (experimental [2]) and for antiprotons (Binary Theory [3]).

ergy loss. At lower projectile velocities, the interaction becomes more and more adiabatic also resulting in reduced energy loss. The dependence of the stopping power on the projectile velocity or corresponding kinetic energy is illustrated on figure 1.1. The figure shows the stopping power of amorphous carbon measured for protons [2] and as predicted by the recently developed Binary Theory for antiprotons [3]. The stopping power curves for other target materials have similar shape. The range where the stopping power reaches its maximum will be refered to as *medium projectile velocities* (or energies). Projectile velocities below that will be refered to as *low velocities* and velocities above that will be refered to as *high velocities.*

Figure 1.1 also reveals a very interesting phenomenon: At low and medium velocities the stopping power of carbon is significantly larger for protons than for antiprotons. This effect is called the Barkas effect and it has been discovered by accident in the 1950'es, when Barkas, Dyer and Heckman measured the mass of Σ-hyperons and K-mesons and noticed, that the range of negative pions through nuclear emulsion was larger than the range of positive pions of the same initial velocity [4]. Today it is widely believed, that this effect is due to polarisation of the target atoms because positive particles attract the electrons in the target material, while negative particles repel them resulting in less interaction compared to the positive particles. Hence, the Barkas effect becomes large at low projectile velocities where the target "has time" to adjust to the projectile.

The availability of low energy antiproton beams at CERN made it possible

to study the Barkas effect around the stopping power maximum. Antiprotons are favoured projectiles in theoretical models, because they are much easier to treat theoretically than protons due the absence of electron capture. This is an important advantage, because charge exchange processes, which are believed to have a significant role in the stopping power, are very difficult to include into the theoretical models.

Extensive measurements have been made for many targets at the Low Energy Antiproton Ring at CERN [5, 6, 7] down to projectile velocities corresponding to the stopping power maximum. The purpose of the experiments presented here was to extend these measurements down to even lower velocities well below the stopping power maximum and study the behaviour of the barkas effect at hitherto unexplored velocities. Choosing a representative set of targets with atomic numbers between 1 and 79, measurements of the stopping powers for antiprotons in the energy range 1-60 keV should contribute significantly to the evaluation of existing and future theories. Such measurements are today possible at the Antiproton Decelerator at CERN, which together with a Radio Frequency Quadrupole Decelerator can deliver antiprotons of 0-120 keV kinetic energy.

Besides it's academic values, a thorough understanding of the energy loss phenomena has many industrial and medical applications. For example in radiation therapy the applied dose to a patient is found as a balance between the required dose to kill a tumour and the maximum dose that healthy human tissue can survive. In order to find the optimal beam, it is important to know the energy loss and range of many ions over a wide energy spectrum.

Radiation damage and protection is also of main concern in space industry. Electronic devices are very sensitive to radiation and have to be protected by proper shielding. On the other hand it is very expensive to send unneccessary weight into space, so an exact knowledge of how much shielding is required to protect the spacecraft can reduce the expenses dramatically.

In the production of semiconductor devices certain impurities have to be implanted into the basis material. These impurities must end up in a narrow region and at an appropriate depth and the desired depth can only be obtained precisely if the corresponding range of the particles is known. As to the required precision I can only mention, that an ordinary computer processor can contain millions transistors on a relatively small area!

Also many types of particle detectors work by recording of how much energy the incoming particles have deposited in the detector. Thus good quantitative knowledge of energy transfers are required in order to make high precision detectors.

Chapter 2

Theory of Stopping Power and Straggling

2.1 Introduction

When a charged particle traverses matter it interacts with the target atoms due to the electromagnetic forces between charged particles. This interaction can be divided into two parts: Elastic collisions with the entire atom and inelastic collisions with the electrons of the target material. While the elastic collisions are two body processes, where momentum is transfered to the target atom as a whole, the inelastic collisions lead to excitation and ionisation of the target atoms. The interactions with the nuclei also lead to angular scattering of the projectiles, see figure 2.1.

Because the electron cloud in an atom is spatially much larger than the atomic nuclei, the inelastic energy loss is expected to be much larger than the elastic energy loss and we shall only be concerned with the inelastic energy loss unless otherwise stated. At very low energies however, the elastic contribution to the total energy loss becomes noticeable and can be as much as 10%-15% of the total stopping power at 1 keV [2, 8].

The elastic part of the total energy loss is usually refered to as nuclear energy loss, while the inelastic part is usually called electronic energy loss. These terms will be used in the rest of this work.

Early investigations of the energy loss of charged particles traversing matter arrive at a general stopping power formula [10]:

$$-\frac{\mathrm{d}E}{\mathrm{d}x} = \frac{4\pi e^4 N Z_2}{m_e v^2} Z_1^2 L \tag{2.1}$$

where N is the target density, Z_2 the target atomic number, m_e the electron mass, v and Z_1 the projectile velocity and charge respectively and L is the socalled "stopping function". Whether classical or quantum mechanics should be applied to describe the interaction depends on the parameter κ introduced
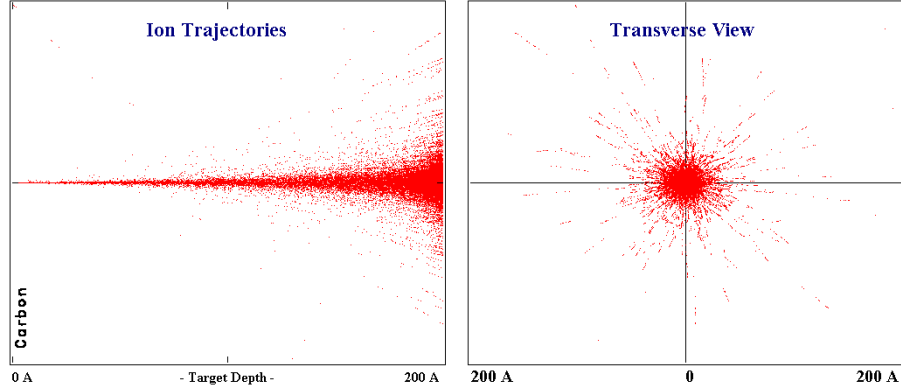
Figure 2.1: Passage of 20 keV protons through 200 Å of carbon. The simulation was done using SRIM [9].

by Bohr [11] in his article on penetration phenomena from 1948. It is given by [10]:

$$\kappa = 2\,|Z_1 Z_2|\,\frac{v_0}{v} \tag{2.2}$$

with $v_0 = \frac{c}{137}$. For scattering by an unscreened Coulomb potential, $\kappa > 1$ make classical mechanics applicable, while $\kappa < 1$ requires a quantum mechanical treatment. When the interaction between projectile and target is sufficiently weak, the interaction can be treated in the first Born approximation. For scattering by a screened Coulomb potential, classical mechanics require a larger κ than the unscreened Coulomb potential, while the first Born approximation is applicable for all screening lengths provided $\kappa < 1$ [10].

Classical mechanics and the first Born approximation can be regarded as two opposite limits of an exact quantum mechanical calculation. Usually, two such limiting cases complement each other, but in this case there is a region for $\kappa > 1$ where screened potentials can't be handled by these methods. In this region a general expansion of the stopping function L in powers of Z_1 can be helpful:

$$L = \sum_{i=0}^{\infty} L_i Z_1^i \tag{2.3}$$

and much of the theoretical work done in this field in the last decades has concentrated on finding coefficients for higher order Z_1 terms.

In the following sections a brief description of various theoretical models will be given.

2.2   Classical Bohr Theory

The first theoretical model for the energy loss of a charged particle penetrating matter was Bohr's classical stopping formula published in 1913. In this

model the energy transfer is divided into nuclear and electronic parts and calculated using classical scattering theory where the stopping medium is described by a harmonic oscillator model. The results are of the form of equation 2.1, namely [10]:

$$-\left(\frac{\mathrm{d}E}{\mathrm{d}x}\right)_{nuc} = \frac{4\pi Z_1^2 Z_2^2 e^4}{M_2 v^2} N L_{nuc} \tag{2.4}$$

$$-\left(\frac{\mathrm{d}E}{\mathrm{d}x}\right)_{elec} = \frac{4\pi Z_1^2 Z_2 e^4}{m_e v^2} N L_{elec} \tag{2.5}$$

with L_{nuc} and L_{elec} given by:

$$
\begin{aligned}
L_{nuc} &= \ln\left(\frac{2a}{b_n}\right) & \text{with} \quad b_n &= \frac{2Z_1 Z_2 e^2}{M_0 v^2} \\
L_{elec} &= \ln\left(\frac{m_e v^3}{2|Z_1|e^2 \overline{\omega}}\right) & \text{with} \quad \overline{\omega} &= (\omega_1 \cdot \omega_2 \cdots \omega_{Z_2})^{\frac{1}{Z_2}}
\end{aligned}
\tag{2.6}
$$

Here a is the target atomic radius, M_2 is the mass of the target, M_0 is the reduced mass of projectile and target and ω_i being a properly chosen binding frequency of the i'th electron in the target atom. These binding frequencies come from the assumption that the force that binds the electrons to the nuclei is harmonic.

As we see from equations 2.4, 2.5 and 2.6, the electronic stopping power calculated in the Bohr theory is independent of the projectile mass and is essentially proportional to both Z_1^2 and $1/v^2$. A rough estimate of the ratio between the electronic and the nuclear stopping powers can also be obtained [10]:

$$\frac{-\left(\frac{\mathrm{d}E}{\mathrm{d}x}\right)_{elec}}{-\left(\frac{\mathrm{d}E}{\mathrm{d}x}\right)_{nuc}} \approx 4000 \frac{L_{elec}}{L_{nuc}} \tag{2.7}$$

where the logarithms are usually equal within a factor of 2.

The Bohr formula for electronic energy loss (equation 2.5) has been found to be in relatively good agreement with experimental data for projectile velocities above the stopping power maximum but not at low velocities where it vanishes and even becomes negative!

2.3 Bethe Theory

As mentioned previously, a relatively simple quantal treatment of the scattering problem can be done if the electromagnetic interaction is weak. For a collision between a charged particle and an atom the Hamiltonian can be written as:

$$H = H_0 + V \tag{2.8}$$

where the interaction potential V may be treated as a perturbation to H_0 and the inelastic energy loss can be calculated in the first Born approximation. This
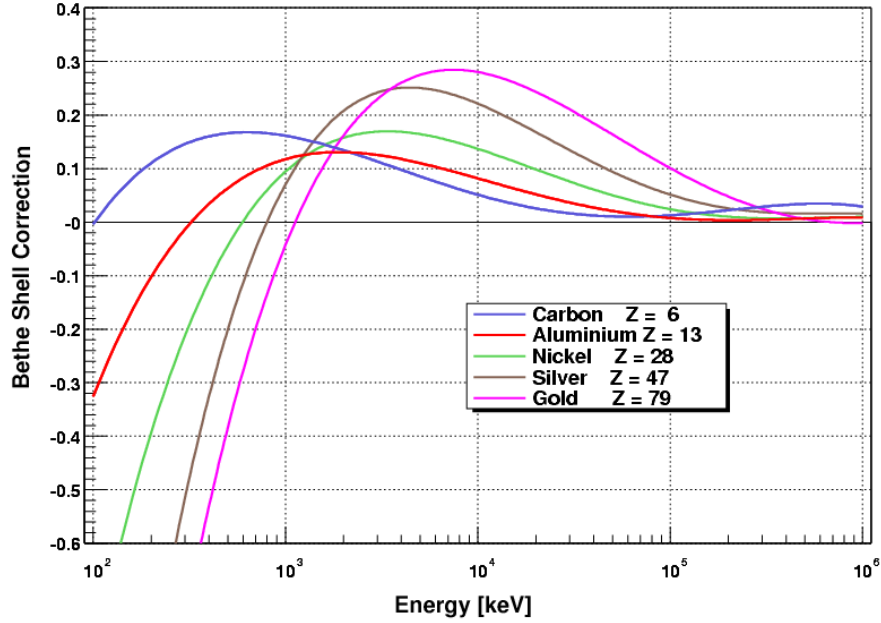
Figure 2.2: The shell correction term (equation 2.13) for a few elements using coefficients deduced in [8]

calculation is done in details in [10] under the assumption, that the target electrons are not displaced significantly during the collision. This is the case for "fast" collisions, where $v \gg v_0$. The obtained formula is:

$$-\frac{\mathrm{d}E}{\mathrm{d}x} = \frac{4\pi Z_1^2 e^4}{m_e v^2} N Z_2 L \qquad (2.9)$$

$$\text{with} \quad L = \ln\left(\frac{2m_e v^2}{I}\right) \qquad (2.10)$$

where I is the mean ionisation potential defined by:

$$\ln I = \sum_n f_n \ln E_n \qquad (2.11)$$

with E_n and f_n being the possible energy transitions and oscillator strengths for the target atom. In practice, equation 2.11 can only be calculated accurately for the simplest atoms but it can be approximated by [10]:

$$I = I_0 Z_2$$

with $I_0 \sim 10\text{eV}$ or extracted from comparisons of the Bethe formula with experimental data as has been done in [8].

When the projectile velocity becomes comparable to the velocity of the inner-shell electrons in the target, $v \gg v_0$ is no longer true and a *shell correction* term is needed. This correction is usually included in the stopping function L which then becomes [11]:

$$L = \ln\left(\frac{2m_e v^2}{I}\right) - \frac{C}{Z_2} \qquad (2.12)$$

The shell correction term should depend on the projectile velocity and become negligible when $v \gg v_0$. It has been deduced in [8] for all elements by fitting the power series:

$$\frac{C}{Z_2} = a_0 + a_1 \ln E + a_2 \left(\ln E\right)^2 + a_3 \left(\ln E\right)^3 + a_4 \left(\ln E\right)^4 \qquad (2.13)$$

to experimental data. The result is plotted for a few elements on figure 2.2 showing the energy and Z_2 dependece.

The Bethe stopping formula with the shell correction has been found to be in good agreement with experimental data in the high velocity region for above the stopping power maximum, but it needs further corrections when the projectile velocity becomes lower or very high.

At lower velocities the interaction between the projectile and the target atoms increases with decreasing projectile velocity and can not be treated as a perturbation. At these projectile velocities, the general expansion of the stopping function (equation 2.3) has been investigated to include higher order terms in Z_1. L_0, which gives a Z_1^2 contribution to the Bethe formula, can be expressed by using equation 2.12. $L_1 Z_1$, which is called the Barkas term, turns out to be important at energies of a couple of MeV and below, where it gives rise to a Z_1^3 contribution to the Bethe stpping power formula, and thus leads to a difference between the energy loss of projectiles of opposite charge. The Barkas term has been calculated using a classical harmonic oscillator model [12, 13] and also using a statistical model for the target atoms [14] arriving at:

$$L_1 = \frac{3\pi}{2} \frac{e^2 \omega}{m_e v^3} \log\left(\frac{v}{1.7\omega a_\omega}\right) \qquad (2.14)$$

with a_ω given approximately by the orbit radius of the electrons in the target atoms or by the quantal radius of the oscillator given by $\sqrt{\hbar/2m_e\omega}$ [14]. This calculation of the Barkas effect assumed *distant* collisions with large impact parameter and did not agree very well the with experimental data from LEAR [5, 6]. Lindhard showed later that the contribution from *close* collisions is of the same significance and added the Z_1^4 term to the Bethe formula [15] which for small κ values can be written as:

$$L_2 = -1.202 \left(\frac{v_0}{v}\right)^2 \qquad (2.15)$$

At very high projectile velocities relativistic corrections are needed to the Bethe formula. This energy region is not relevant for the present experiments and I will not go into details but just mention, that the relativistic Bethe formula can be written as [11]:

$$-\frac{dE}{dx} = \frac{4\pi e^4 N Z_2}{m_e c^2 \beta^2} Z_1^2 \left[\ln\left(\frac{2m_e c^2 \beta^2 \gamma^2}{I}\right) - \frac{C}{Z_2} - \beta^2 - \frac{\delta}{2}\right] \qquad (2.16)$$
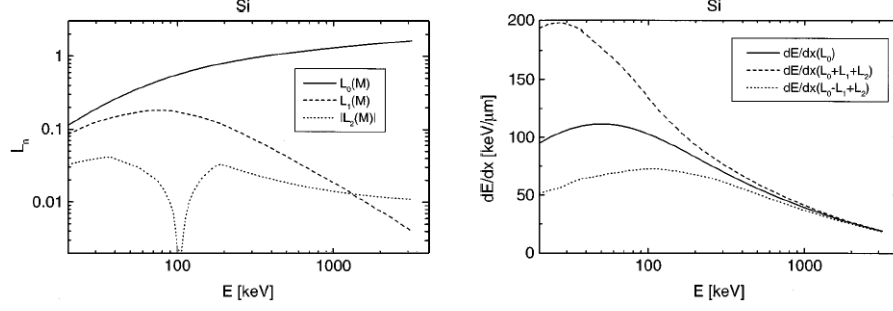
Figure 2.3: **Left:** The first three terms of the stopping function L calculated in the quantal harmonic oscillator model for the M shell in Si. **Right:** The corresponding stopping power including only the Z_1^2 term (solid curve) and including the Z_1^3 and Z_1^4 terms for protons (dashed curve) and antiprotons (dotted curve). The figures are from [7].

2.4   Quantal Harmonic Oscillator

As mentioned previously, the Bohr and Bethe theories can be thought of as two limiting cases of an exact quantum calculation. The Bohr theory uses classical scattering theory and describes the stopping medium as a harmonic oscillator. In the Bethe theory the interaction between projectile and target is calculated using the first Born approximation, whereafter higher order terms are added to the stopping function L in order to correct for it's flaws.

In the quantal harmonic oscillator model these methods are combined by using a harmonic oscillator model for the stopping medium and calculating the interaction within the first Born approximation as done by Sigmund and Haagerup [16]. Later, these calculations have been extended to second order as well [17].

In a numerical solution of the time dependent Schrödinger equation, Mikkelsen and Flyvbjerg [18] also used the quantal harmonic oscillator model to describe the stopping medium. These calculations are accurate within the limits of the harmonic oscillator in the sense that no further assumptions are made.

Results of the quantal harmonic oscillator calculations have been compared previously to experimental data from LEAR [6, 7] and were found to be in fair agreement around the stopping maximum for many materials. The model has the ability to give a good estimate of the barkas contribution to the stopping power and it shows, that the Barkas term becomes very large at the stopping maximum, see figure 2.3.

2.5 Electron Gas Models

Relatively simple formulas describing both nuclear and electronic energy loss at low velocities have been obtained by Lindhard and Scharff for power potentials by using classical mechanics and describing the target locally as an electron gas [19]. The stopping cross sections per atom using a Thomas-Fermi potential ($\sim r^{-2}$) have been found to be:

$$S_{nuc} = 0.416 \cdot \pi^2 e^2 a Z_1 Z_2 \frac{M_1}{M_1 + M_2} \tag{2.17}$$

$$S_{elec} = Z_1^{\frac{1}{6}} 8\pi e^2 a_0 \frac{Z_1 Z_2}{\left(Z_1^{\frac{2}{3}} + Z_2^{\frac{2}{3}}\right)^{\frac{3}{2}}} \cdot \frac{v}{v_0} \tag{2.18}$$

with $a = 0.8853 a_0 \left(Z_1^{\frac{2}{3}} + Z_2^{\frac{2}{3}}\right)^{-\frac{1}{2}}$ and a_0 being the Bohr radius. We see that in this model the electronic stopping is proportional to the projectile velocity while the nuclear contribution is constant. The nuclear stopping should therefore become more significant with decreasing projectile velocity. This model is only valid at low and medium projectile velocities below the stopping power maximum, namely when:

$$v < v_0 Z_1^{\frac{2}{3}} \tag{2.19}$$

Although equation 2.18 is only an approximate formula, it is expected to give accurate results down to low projectile velocities, even for $v \ll v_0$ where the Bohr and Bethe formulas fail.

Later when the Barkas effect was measured with protons and antiprotons down to velocities corresponding to 500 keV [5] and found to increase with decreasing projectile velocity, another similar model was developed by Sørensen [20] to investigate it's behaviour below the stopping power maximum. Here the target electrons are described as a degenerate, homogeneous Fermi gas, and the stopping power maximum is expected to occur near the Fermi velocity, v_F. The final stopping formula in the limit $v \ll v_F$ reads:

$$-\frac{\mathrm{d}E}{\mathrm{d}x} = \frac{4}{3\pi} Z_1^2 C\left(\chi\right) \frac{v}{v_0} \frac{e^2}{a_0^2} \tag{2.20}$$

where χ is the density parameter given by $\chi \equiv \sqrt{\frac{v_0}{\pi v_F}}$ and is assumed to be less than 1. $C\left(\chi\right)$ is the stopping function which in a second order Born approximation can be expressed as $C = C_1 + C_2$ with:

$$C_1 = \frac{1}{2}\left[\ln\left(\frac{1+\chi^2}{\chi^2}\right) - \frac{1}{1+\chi^2}\right] \tag{2.21}$$

$$C_2 = \frac{2\pi Z_1 \chi^3}{3 + 4\chi^2}\left[4 \cdot \left(1+\chi^2\right) \cdot \ln\left(\frac{\frac{1}{4}+\chi^2+\chi^4}{\chi^2+\chi^4}\right) - \ln\left(\frac{1+\chi^2}{\chi^2}\right)\right] \tag{2.22}$$

As we see, this model also predicts a velocity proportional behaviour of the energy loss and the only unknown parameter is the density parameter χ. One can, however, estimate the values of C_1 and C_2 by averaging $C_1(\chi)$ and $C_2(\chi)$ using electron densities of the target atoms [20].

It should be noted, that equations 2.21 and 2.22 only give reasonable estimates of the stopping power for small values of χ. When χ becomes larger than approximately 0.4, this second order Born approximation gives too high Barkas corrections. For these values of χ, a quantum mechanical computation of the stopping function C can be done [20].

2.6   Binary Theory

The binary theory of electronic stopping has been developed recently by Sigmund and Schinner as an attempt to quantify the stopping of swift heavy ions in various materials over a wide energy range [21]. They have now also applied the theory to light ions including protons and antiprotons [3, 22].

The binary theory is an extension to Bohr's classical theory described in section 2.2, where the original harmonic potential in which the target electrons are bound, is replaced by an effective screened potential. The theory assumes binary collisions between projectile and target and includes all the necessary corrections for both low and high projectile velocities.

In the case of antiprotons, the stopping power can be written as in the Bohr theory:

$$-\frac{\mathrm{d}E}{\mathrm{d}x} = \frac{4\pi Z_1^2 Z_2 e^4}{m_e v^2} N L \tag{2.23}$$

but instead of expanding L as in equation 2.3 it is written in the form [3]:

$$L = L_{bin} + \Delta L \tag{2.24}$$

where L_{bin} describes the low velocity behaviour as predicted by the binary theory for heavy ions and ΔL is a correction term that becomes significant at high velocities. In practice, L_{bin} is calculated numerically using weighted atomic oscillator frequencies as input which are obtained from optical properties of the target atoms [21]. Once a correct set of optical parameters are found, the binary theory should not need any other input parameters.

The binary theory for electronic stopping has been compared to many existing experimental data sets. There seems to be very good agreement for a wide variety of projectile-target combinations with projectile energies spanning over 6 decades.

2.7   Energy Loss Straggling

Due to the statistical nature of atomic collisions, the energy loss of originally mononergetic particles while passing through matter fluctuates around an aver-

age energy loss $(\overline{-\Delta E})$. This is known as Energy Loss Straggling. The average energy loss, defined in terms of the stopping cross section is:

$$\overline{\Delta E} = N\Delta x S = N\Delta x \int T \frac{\mathrm{d}\sigma}{\mathrm{d}T} \mathrm{d}T \qquad (2.25)$$

where T is the energy transfer during collision, $\frac{\mathrm{d}\sigma}{\mathrm{d}T}$ is the cross section for energy transfer T and Δx is the path length of the projectile through the stopping medium. The average square fluctuation is then given by:

$$\Omega^2 \equiv \overline{\left((-\Delta E) - (\overline{-\Delta E})\right)^2} = N\Delta x \int \mathrm{d}T \frac{\mathrm{d}\sigma}{\mathrm{d}T} T^2 \qquad (2.26)$$

In the classical Bohr theory (section 2.2) one obtains by using the Rutherford cross section [10]:

$$\Omega^2_{nuc} = 4\pi Z_1^2 Z_2^2 e^4 \left(\frac{M_1}{M_1 + M_2}\right)^2 N\Delta x \qquad (2.27)$$

$$\Omega^2_{elec} \approx 4\pi Z_1^2 Z_2 e^4 N\Delta x \qquad (2.28)$$

provided the target electron velocities are negligible compared to the projectile velocities. For the case of proton projectiles passing through a heavy target, $Z_2 \gg Z_1 = 1$, one finds the ratio between the nuclear and electronic contributions to be:

$$\frac{\Omega^2_{elec}}{\Omega^2_{nuc}} \approx 4 \cdot Z_2$$

At low projectile velocities, where the Bohr formulas are not expected to be correct, calculations using the electron gas model can be used to describe the energy straggling. This has been done by Lindhard and Scharff [23] and they arrived at:

$$\Omega^2 = \Omega^2_B \cdot \frac{1}{2} \left[1.36 \frac{v}{v_0} \frac{1}{\sqrt{Z_2}} - 0.016 \left(\frac{v}{v_0}\right)^3 \frac{1}{Z_2^{\frac{3}{2}}}\right] \qquad (2.29)$$

where Ω_B is the result obtained in the classical Bohr model (equation 2.28). This result is valid if $v < \sqrt{3Z_2}v_0$. Later Bonderup and Hvelplund refined this by using a Lenz-Jensen atomic model and obtained [24]:

$$\frac{\Omega^2}{\Omega^2_B} = \frac{1}{Z_2} \int_0^\infty \mathrm{d}r 4\pi r^2 \rho(r) \frac{\Omega^2(r,v)}{\Omega^2_B} \qquad (2.30)$$

with:

$$\frac{\Omega^2(r,v)}{\Omega^2_B} = \begin{cases} 1 + \left(\frac{1}{5} + \frac{\chi(r)}{\sqrt{3}}\right)\left(\frac{v_F(r)}{v}\right)^2 \ln\left(\frac{v}{v_F(r)}\right)^2 & \text{if } v \gtrsim v_F(r) \\[2ex] \frac{1}{\sqrt{1+13\chi^2}}\left(\frac{v}{v_F(r)}\right)^2 & \text{if } v \lesssim v_F(r) \end{cases} \qquad (2.31)$$

Here $v_F(r)$ and $\chi(r)$ can be expressed in terms of the electron density $\rho(r)$ which in turn is found from the Lenz-Jensen model for the atom. The Lindhard-Scharff and Bonderup-Hvelplund calculations are based on the random-phase

approximation theory which is not valid for metal electron gasses [25] and thus can not be expected to give accurate values for such targets. This is not the case for the formula obtained by Wang and Ma where the energy loss straggling is expressed as [25]:

$$\frac{\mathrm{d}\Omega^2}{\mathrm{d}x} = 6.889 \cdot 10^{-5} C\left(r_s\right) \quad \left[\frac{\mathrm{keV}^2}{\mathrm{\AA}}\right] \tag{2.32}$$

The values of C are tabulated in [25] as a function of r_s the radius of the free electron sphere in the target material [26].

Although the Wang-Ma formula is expected to give accurate results at low projectile velocities, it still needs further corrections, because in a real target, the electrons do not constitute a homogeneous gas. They are bunched into atoms, which might again be bunched in molecules or a crystal lattice. There might also be a texture effect coming from inhomogeneties in the thickness of the target material. All these correlations lead to extra energy loss straggling that should be included. A detailed study of these effects has been reported by Besenbacher et al. [27] arriving at:

$$\Omega_A^2 = N\Delta R \frac{S^2}{\pi r_A^2} \tag{2.33}$$

$$\Omega_M^2 = N\Delta R \frac{S^2}{\pi d^2} \tag{2.34}$$

where Ω_A and Ω_M is the straggling due to the atomic or the molecular correlation resplectively, S is the stopping cross section, r_A is the atomic radius and d is the internuclear distance in the molecule. For small internuclear distances one obtains $\Omega_A = \Omega_M$. The effective atomic area can ususally be approximated by $\pi r_A^2 \approx 10\pi r_0^2$ but Besenbacher et al. showed that the effective atomic area is increasing as the projectile velocity decreases and is larger than $10\pi r_0^2$ for $v < v_0$ [27].

As for the target thickness inhomogeneties, Besenbacher et al. found, that if the foil thickness distribution is a Gaussian with standard deviation σ_x, the extra contribution to the energy loss straggling can be written as:

$$\Omega_{\sigma_x}^2 = \left(\frac{\mathrm{d}E}{\mathrm{d}x}\right)^2 \sigma_x{}^2 \tag{2.35}$$

Texture effects are important when projectiles have high atomic numbers and low velocities.

One important question remains, namely the energy *distribution* of the projectiles after they have traveled through the target. It has been show by Bonderup [10] that for electronic energy loss, the energy distribution is a Gaussian with mean $\left(\overline{-\Delta E}\right)$ and root mean square width Ω:

$$P\left(E\right) = \frac{1}{\sqrt{2\pi\Omega^2}} \cdot \exp\left(-\frac{\left(E - \left(\overline{-\Delta E}\right)\right)^2}{2\Omega^2}\right) \tag{2.36}$$

It is however also shown, that nuclear collisions can be very strong with much larger energy losses than $(\overline{-\Delta E})$ causing an assymetry in the Gaussian. These violent nuclear collisions are expected to be very infrequent thus the assymetry is only seen in the tails of the Gaussian.

Chapter 3

Apparatus

The apparatus for measuring stopping power and straggling consists of an electrostatic spectrometer which measures the energy of the beam before and after the target foil or gas. The spectrometer has been designed to measure electronic stopping power for (anti)protons, nevertheless it can be used with other charged particles as well. Details of the spectrometer are given in section 3.4.

The spectrometer has been tested and calibrated with a proton accelerator in Århus with beam energies up to 30 keV (see section 3.3).

The measurements with antiprotons have been carried out at the Antiproton Decelerator (AD) at CERN as part of the ASACUSA collaboration [28]. The AD is a new low energy antiproton facility replacing the previous antiproton complex which consisted of the Proton Syncrotron (PS), Antiproton Accumulator (AA), Antiproton Collector (AC) and the Low Energy Antiproton Ring (LEAR) [29].

The antiprotons are created by a 26 GeV/c proton beam coming from the PS and hitting an iridium target. Approximately $5 \cdot 10^7$ antiprotons at 3.57 GeV/c[1] are collected by a magnetic horn and decelerated in the AD ring to 100 MeV/c which corresponds to a kinetic energy[2] of 5.31 MeV, see section 3.1. After extraction from the AD, the antiprotons are post-decelerated using a newly constructed *Radio Frequency Quadrupole Decelerator* (RFQD) to a kinetic energy of 0..120 keV (see section 3.2). The RFQD has been tested with protons in Århus in September 2000.

---

[1]The produced antiprotons have a wide momentum distribution centered around 3.57 GeV/c [30].

[2]The relation between momentum and kinetic energy in relativistic terms is $E_{kin} = E_{tot} - E_0 = \sqrt{(pc)^2 + (m_0 c^2)^2} - m_0 c^2$, where p is the momentum, m_0 the rest mass and c the speed of light.

17
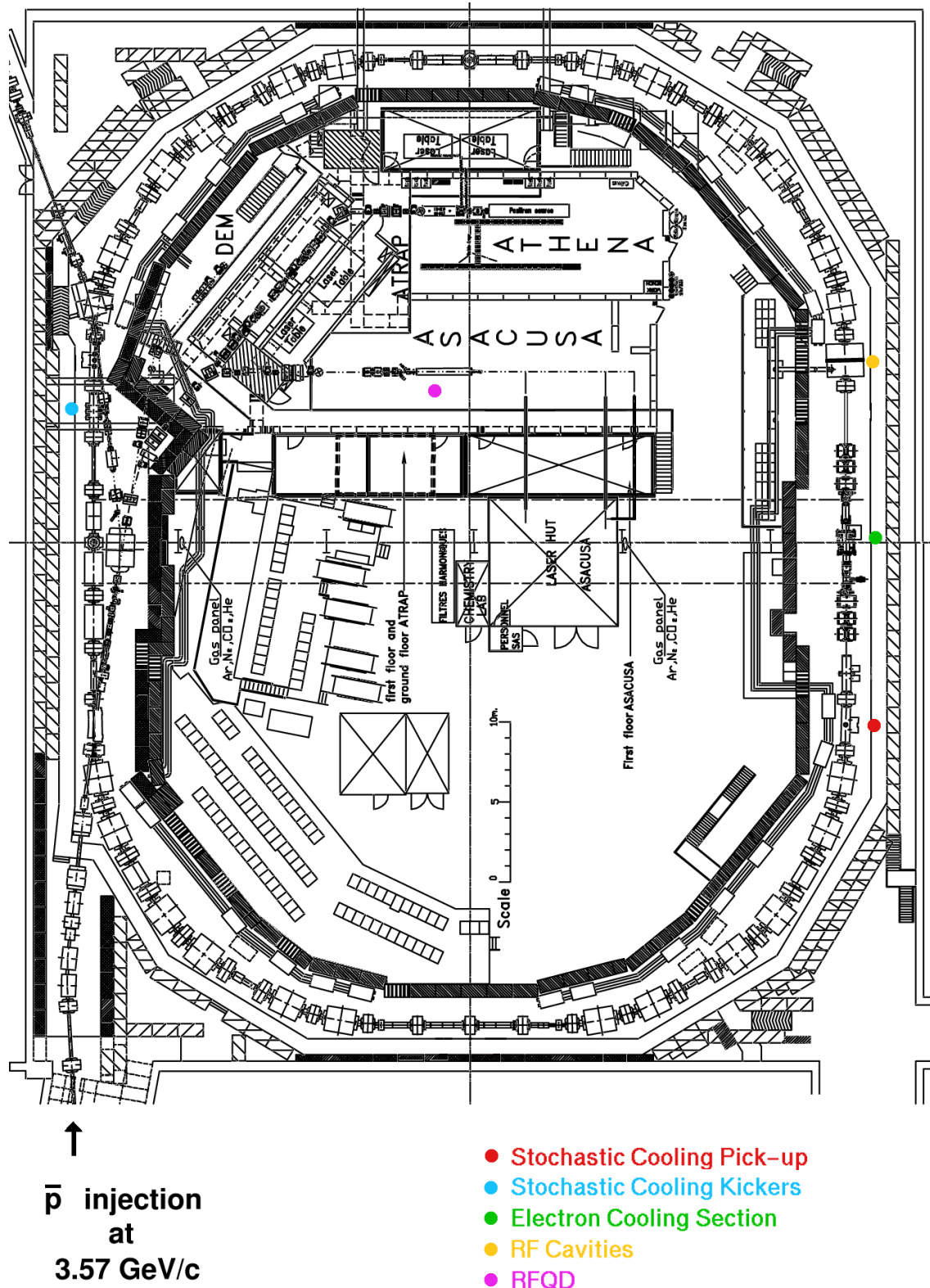
Figure 3.1: Schematic drawing of the antiproton decelerator and its experimental areas. The figure is from [31] and slightly modified.
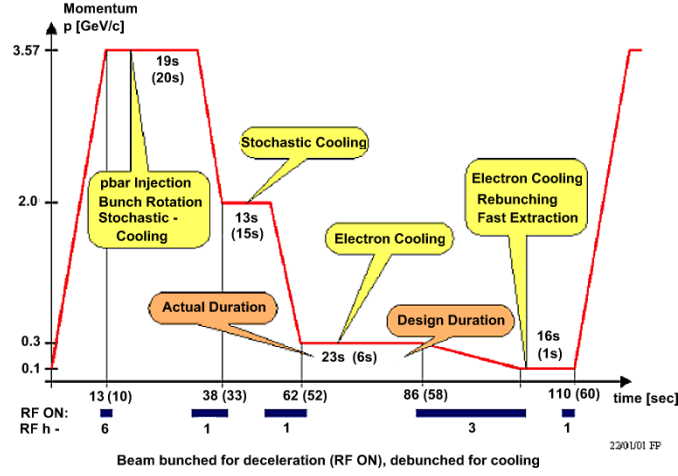
Figure 3.2: The AD cycle. The numbers in brackets indicate the estimated durations. The figure originates from [34].

3.1 Antiproton Decelerator

The collected antiprotons are bunch rotated[3] whereby the momentum dispersion is reduced from $\pm 3\%$ to $\pm 0.75\%$ [32]. The transverse emittances[4] are then reduced to 5πmm·mrad using stochastic cooling and the antiprotons are decelerated in three steps, see figure 3.2. The deceleration is done using electromagnetic waves (reversed accelerator) at frequencies between 0.5 and 1.59 MHz and the system, including the cavities, is a modified version of the old RF system from the AC. The antiprotons are decelerated by 212 eV per turn [33].

During deceleration, the transverse beam emittances increase dramatically and to counteract this, the beam is cooled after each deceleration step. This is illustrated by the flat areas on figure 3.2. At high energies the beam is cooled using stochastic cooling, where deviations from the ideal orbit are corrected using a kicker magnet. The idea is illustrated i figure 3.3, see [35, 36] for details. At lower energies electron cooling is applied, where a cold electron beam is merged with the antiproton beam. Part of the transversal energy of the antiprotons is transfered to the electrons [35, 37], and after a short distance (few meters) the electrons are removed again using a magnet. Because of the large difference between electron and antiproton masses the magnet will essentially only affect the electron path.

Effective electron cooling needs precise overlap between the electrons and antiprotons, which is why electron cooling at the AD is much slower than ex-

---

[3]Bunch rotation is a rotation in the longitudinal phase space, where a short pulse with large energy spread is rotated to a long pulse with small energy spread.

[4]Emittance is the area of an ellipse in the transversal phase space with coordinates (x, x') or (y, y'), containing 95% of the particles.
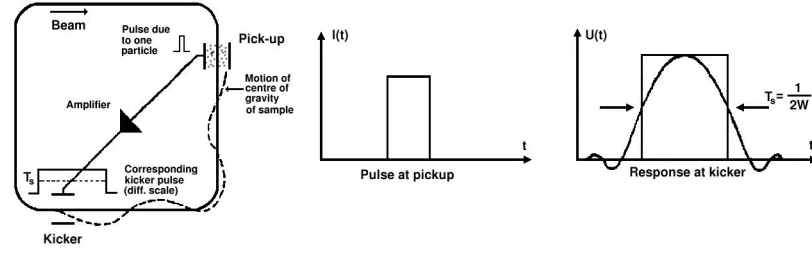
Figure 3.3: The principle in stochastic cooling [36].
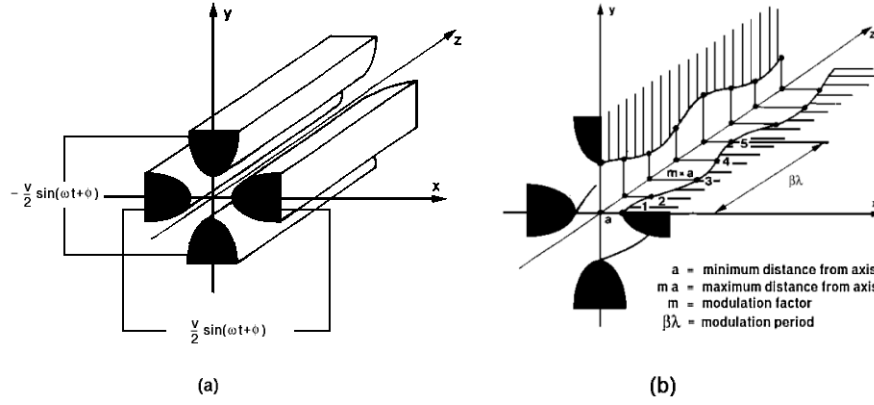
Figure 3.4: (a) Electric quadrupole electrodes (focusing). (b) Modulated quadrupole electrodes (focusing and accelerating). The drawings are from [38].

pected. On the contrary, stochastic cooling has turned out to be much more effective than expected and the final emittances after the stochastic cooling stages are smaller than expected, see table A.2 in appendix A. The total AD deceleration period is almost two minutes, twice as long as the designed period. Details are given in tables A.1 and A.2 in appendix A.

3.2   Radio Frequency Quadrupole Decelerator

3.2.1   Principles of an RFQ Accelerator

Since their invention in 1970, RF quadrupoles have been very popular low-energy accelerators because of their ability to accelerate and focus the beam with the same electromagtic field [38]. The idea is to put alternating voltage on four electrodes along the longitudinal axis, see figure 3.4a. The voltage oscillates with a relatively high frequency, typically 100..400 MHz, and those particles which are slow enough to stay inside the quadrupole for several oscillator periods, are exposed to an oscillating transverse electric field and thus focused in the same way as when passing through several quadrupole magnets with changing polarities.

By modifying the electrodes to a sinusoidal form, part of the transverse field is turned into the longitudinal direction creating an accelerating field, see figure 3.4b. This modification of the electrodes is called *modulation* and the modulation period is equal to $\beta\lambda$, β being the relativistic factor v/c and λ being the wavelength of the RF field. The modulation period is not constant along the RFQ because the velocity of the particles increases gradually.

Two opposite electrodes in an RFQ can be displaced in different ways to obtain different functions of an RFQ. Two examples are shown on figure 3.5, where the first one is used for acceleration while the second is used to merge two parallel beams [38].
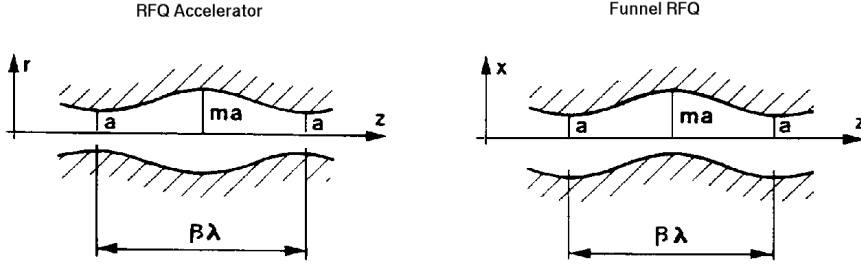
Figure 3.5: RFQ electrodes.

The fields in an RFQ can be described by solving the Laplace equation, which in cylindrical coordinates is:

$$\nabla^2 U\,(r,\theta,z) = \frac{1}{r}\frac{\partial}{\partial r}\left(r\frac{\partial U}{\partial r}\right) + \frac{1}{r^2}\frac{\partial^2 U}{\partial\theta^2} + \frac{\partial^2 U}{\partial z^2} = 0 \qquad (3.1)$$

where $U\,(r,\theta,z)$ is the potential in the RFQ. The general solution is [38]:

$$U\,(r,\theta,z) = \frac{V}{2}\left[\sum^{n} A_{0n}r^{2n}\cos(2n\theta) + \sum^{n,m} A_{mn}I_{2n}(mkr)\cos(mkz)\right] \qquad (3.2)$$

where $m + n = 2p + 1$ with $p = 0, 1, 2, ...,$ V is the electrode voltage (as shown on figure 3.4a), $I_{2n}(x)$ are the modified Bessel functions, $k = 2\pi/\beta\lambda$ and A_{mn} are constants determined from the boundary conditions. To lowest order[5] this gives:

$$U\,(r,\theta,z) = \frac{V}{2}\left[A_{01}r^2\cos(2\theta) + A_{10}I_0\,(kr)\cos(kz)\right] \qquad (3.3)$$

which includes a transverse component (electric quadrupole potential) and a longitudinal component (acceleration). The corresponding electric field is

$$\begin{aligned}
E_r &= -\frac{\partial U}{\partial r} &&= -\frac{V}{2}\left[2A_{01}r\cos(2\theta) + kA_{10}I_1(kr)\cos(kz)\right]\\
E_\theta &= -\frac{1}{r}\frac{\partial U}{\partial\theta} &&= VA_{01}r\sin(2\theta) && (3.4)\\
E_z &= -\frac{\partial U}{\partial z} &&= \frac{V}{2}kA_{10}I_0\,(kr)\sin(kz)
\end{aligned}$$

---

[5]An RFQ is usually well described with only few harmonics.

3.2.2   RFQ Decelerator

The idea with a decelerating RFQ is to transfer the focusing property of an
RFQ to a decelerator and thus have both deceleration and transport in the same
element. The result is a compact machine with a relatively high deceleration
efficiency: The CERN RFQD, which is the first functional RFQ decelerator,
is approximately 4 m long and can decelerate protons or antiprotons from 5.3
MeV to 0..120 keV.

A decelerating RFQ can not be thought of as a reverse RFQ accelerator,
because the longitudinal acceptance of the decelerator decreases gradually with
the decreasing particle velocity [38, 39]. Therefore the decelerator needs a good
match of the phase space at the entrance, which can be obtained either with
non-accelerating RFQ cells or a conventional RF cavity placed before the RFQD
[39]. To use RFQ cells for matching is not optimal because the high energy at the
entrance of the RFQ requires long cells which then would result in a very long
machine (17m in the present case). Any compromise in this matter would reduce
the efficiency which mainly depends on the longitudinal matching. The CERN
RFQD uses therefore a conventional RF cavity placed 6.15 meter upstream from
the RFQD [40].

As mentioned before, the shape of the RFQ electrodes depends on the ve-
locity of the particles (the modulation factor is equal to $\beta\lambda$), so the input and
output velocities of an RFQ are fixed. To obtain decelerated particles with vari-
able energy, the vanes in the CERN RFQD have been isolated from the tank
and can be biased up to ± 60 kV, see figure 3.6. This applied bias (also called
ladder voltage) also changes the optimal input energy, which is why an energy
corrector cavity has been added at the entrance of the RFQD [40].
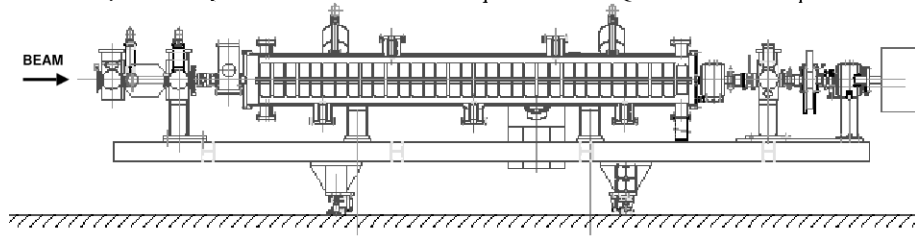
Figure 3.6: The CERN RFQ decelerator seen from the side [40].

The focusing of the RFQ is not sufficient to deliver a parallel decelerated
beam. It is therefore necessary with external focusing elements after the RFQ,
which in this case are a set of solenoids.

The theoretical deceleration efficiency of the CERN RFQD is 45% and most
of the undecelerated beam passes straight through the RFQ with an unchanged
energy of 5.3 MeV. Other key parameters are given in table A.3 in appendix A.
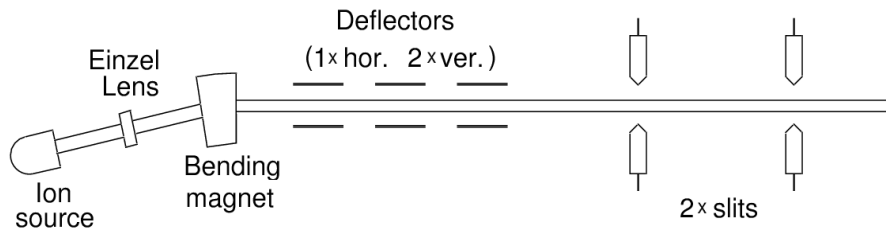
Figure 3.7: Schematic layout of the 0..30 keV proton accelerator (not in scale).
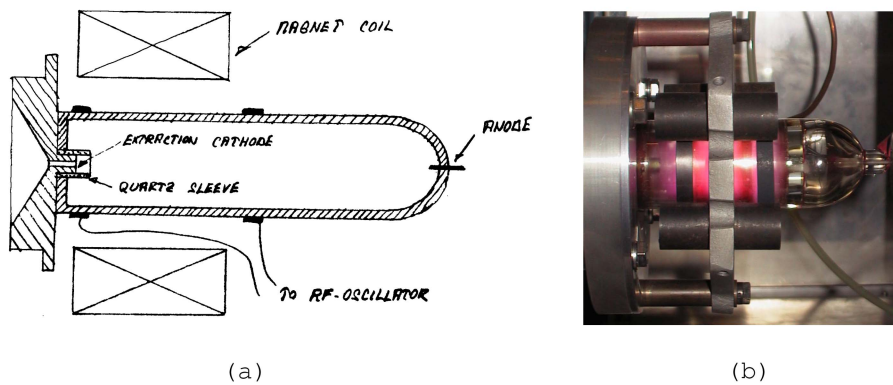
Figure 3.8: (a) Schematic drawing of a radio frequency ion source. (b) Picture of our RF ion source. Recombination of hydrogen (H_β og H_γ) gives the purple color. The drawing is from [41].

3.3 Proton Accelerator

This accelerator has been used to test and calibrate the electrostatic spectrometer by measuring the stopping power and straggling of protons. The accelerator consists of a radio frequency ion source, an acceleration gap, a bending magnet and some additional elements to steer and focus the beam, see figure 3.7.

The ions are created by ionization of a gas using a radio frequency field. The plasma is created in a cylindrical glas container, where the gas[6] is let in at a pressure of 10^{-3} to 10^{-2} mbar, see figure 3.8. The radio frequency field is applied via two metallic rings placed around the glas container. The oscillator frequency is around 100 MHz and the transfered power is approximately 50..75 Watts. This type of ion source has low power consumption and long lifetime, but can only be used to produce ions from gasses. The applied radio frequency field makes the electrons in the gas oscillate and their energy will gradually increase. To make this *heating* more effective, a magnetic field is applied parallel to the

---

[6]To obtain protons one uses hydrogen gas.

RF field to keep the electrons within the range of the RF field. This magnetic field can be obtained by placing a solenoid outside the glas container. When the energy of the electrons become sufficiently large the electrons detach from the protons creating a plasma.

Extraction is done by applying a positive voltage on the anode placed at the opposite end from the extraction cathode. The extraction cathode is made of a cylindrical aluminium tap with a hole in the middle and is surrounded by a quartz tube to isolate the cathode from the plasma. By choosing a proper geometry for the aluminium tap and the quartz tube, the extracted protons can be focused through the extraction channel.

The construction is biased with a positive voltage between 0..30 kV giving extra kinetic energy to the extracted protons.

3.4   The Electrostatic Spectrometer

3.4.1   Basic Overview

The main parts of the electrostatic spectrometer are two electrostatic analysers (bending sections) with the target placed in between them, see figure 3.9. The first analyser, ESA-1, determines the projectile energy before the target, while the second, ESA-2, determines the projectile energy after passage through the target. The first analyser is necessary because of the large energy spread of the RFQD and to avoid the direct background from the 5.3 MeV antiprotons, cf. section 3.2. The analyzers have fixed positions and only projectiles transmitted in the forard direction through the target will be transmitted through the second analyzer. Thus the spectrometer is expected only to measure the electronic contribution to the total energy loss.

The surface of the analyser electrodes is made spherical to obtain horizontal and vertical focusing, see figure 3.10a.

The spectrometer can be used to measure energy loss of both protons and antiprotons. Changing between the two modes is done by changing the polarity of the power supplies.

The force required to keep a particle with mass m, velocity v and charge q in a circular orbit with radius R is:

$$F = \frac{mv^2}{R} = qE_0 \tag{3.5}$$

where E_0 is the magnitude of the electric field in the middle between the two electrodes. The electric field is given by [43]:

$$
\begin{aligned}
E(r) &= E_0 \left(\frac{R}{r} \right) \\
&\cong E_0 \left(1 - \frac{2x}{R} \right) \qquad \text{for } R \gg d, x = r - R
\end{aligned}
\tag{3.6}
$$
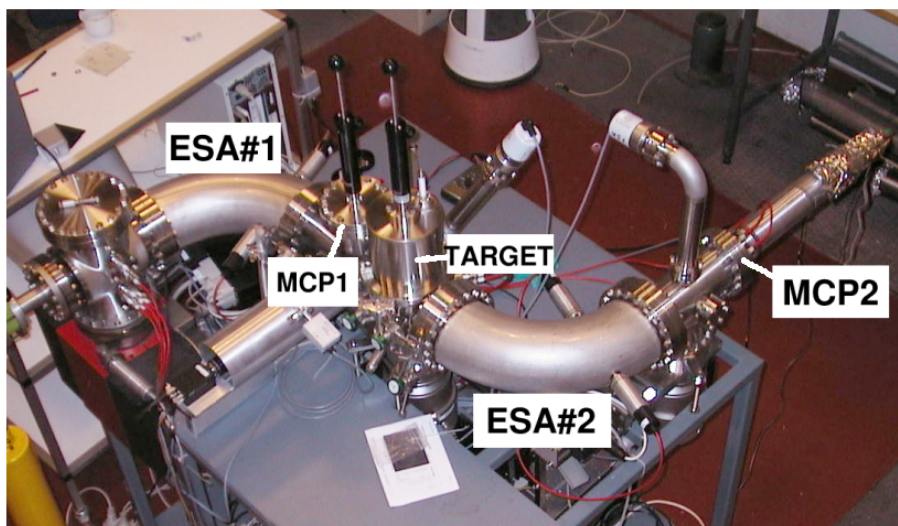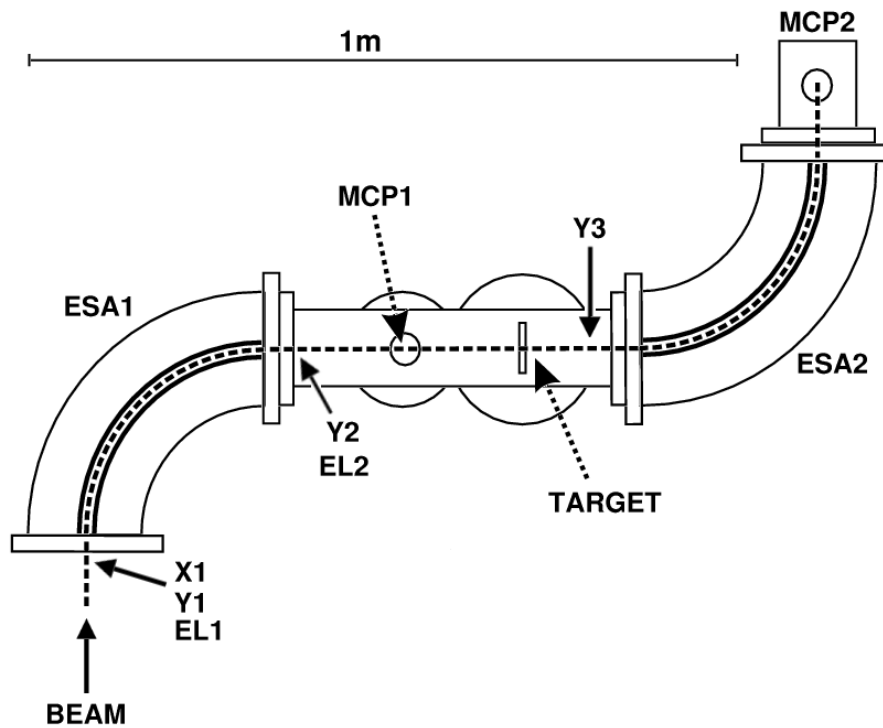
Figure 3.9: Schematic layout and picture of the electrostatic spectrometer.
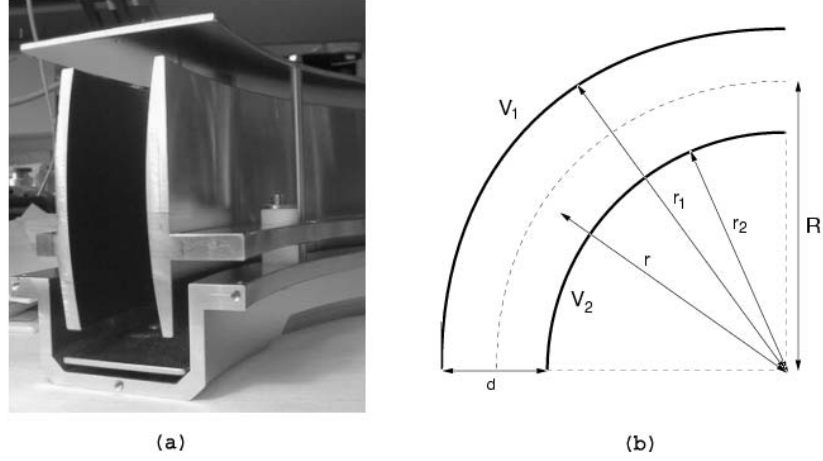
Figure 3.10: (a) Picture of an electrostatic analyser with spherical electrodes. The analyser is from ELISA which is a storage ring with only electrostatic optics, see [42]. (b) Schematic drawing of an electrostatic analyser showing the symbols from the text.

where r is the orbit radius of a particle travelling through the analyser (see figure 3.10b). If the voltage difference between the two electrodes is ΔV, the magnitude of the electric field in the middle of the analyser becomes:

$$
\begin{aligned}
E_0 &= \frac{\Delta V}{d} \cdot \left(1 - \frac{d^2}{4R^2}\right) \\
&\cong \frac{\Delta V}{d} = \frac{V_1 - V_2}{r_1 - r_2}
\end{aligned}
\tag{3.7}
$$

and the corresponding kinetic energy a particle needs to pass through the analyser:

$$
\begin{aligned}
E_{kin} &= \frac{1}{4} e \left(V_1 - V_2\right) \frac{r_1 + r_2}{r_1 - r_2} \\
&= \Delta V e \frac{R}{2d}
\end{aligned}
\tag{3.8}
$$

Particles with kinetic energies different from E_{kin} will deviate from the ideal orbit at the exit of the analyser. We can get an estimate of the maximal energy spread at the exit of an analyser from equation 3.8:

$$
\Delta E_{kin} = \frac{d}{2R} E_{kin}
\tag{3.9}
$$

If the energy of a particle deviates more than that, it will not reach the exit of the analyser but hit one of the electrodes instead. Note that this simple calculation assumes that the particles enter the analyser tangentially in the middle of the two electrodes.

To reduce the energy spread even more, there is a possibility to insert a small aperture after ESA-1 and one before ESA-2. We have not used them though,

because they also reduce the transmission through the whole setup.

With the actual choice of parameters for R (250 mm) and d (20 mm), the relation between kinetic energy and voltage difference between the two electrodes becomes (cf. equation 3.8):

$$E_{kin} \ [\text{keV}] = 6.25 \cdot \Delta V \ [\text{kV}] \tag{3.10}$$

The voltage on each electrode can be varied between 0..8 kV ($\Delta V = 16\text{kV}$) giving an energy range of 0..100 keV.

Table A.4 in appendix A contains a listing of the physical parameters for the electrostatic spectrometer.

3.4.2 Steering and Focusing

How well the particles pass through the spectrometer depends on the beam quality at the entrance. To correct for small deviations from the optimal orbit a set of horizontal and vertical deflector plates have been placed before the entrance of the first analyser (X_1 and Y_1 on figure 3.9). The bending angle of the deflectors is given by [43]:

$$\alpha = \frac{\Delta V L}{2 d E_{kin}} \tag{3.11}$$

where L is the length of the plates and d is the distance between two parallel plates. There are two more vertical deflector plate sets after the first analyser, one before and one after the target (Y_2 and Y_3 on figure 3.9). There are no other horizontal deflectors than X_1 because horizontal steering after the first analyser would introduce systematic errors in the energy measurements.

In order to move the focal point between the two analysers, an Einzel lens has been placed at the entrance of the first analyser (EL1 on figure 3.9). This is necessary because the target is not in the middle of the two analysers. The Einzel lens is made out of three co-axial cylindrical electrodes, where the outer electrodes are grounded and a variable voltage V is applied to the inner electrode. The focal length for such an Einzel lens is approximately [43]:

$$f = 0.91 \cdot \frac{D E_{kin}}{V} \tag{3.12}$$

where D is the lens diameter and the electrode separation is $D/10$. Positive voltage is used for protons and negative voltage for antiprotons.

There is an Einzel lens at the exit of the first analyser as well (EL2 on figure 3.9) but it has a very limited effect at higher energies because of the short distance to the target.

3.4.3 Detectors

In order to measure energy distributions of particles we need detectors that can tell us the beam intensity. We have chosen a two stage *Micro Channel Plate* (MCP), which has the advantage of giving a visible picture of the beam.
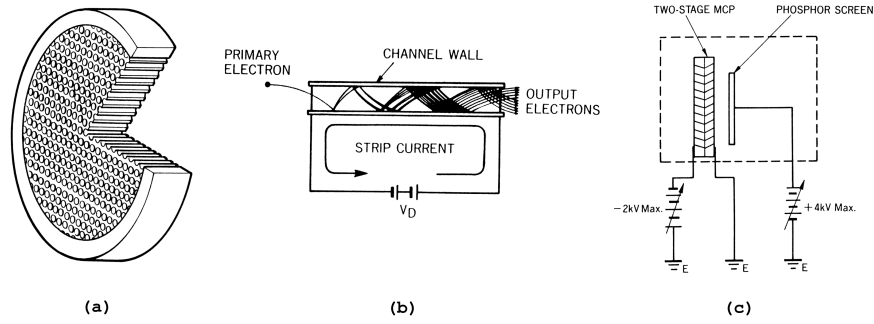
Figure 3.11: (a) Drawing of an MCP. (b) The working principle in an MCP channel. The gain goes like $\sim \exp(V_D)$ up to a certain limit [45]. (c) Two stage MCP configuration with a phosphor screen. The channels are tilted $8°$ to eliminate ion feedback. The gain of the detector can be adjusted by variation of the applied voltage. The drawings originate from [45].

An MCP consists of a glas or ceramic plate with many electron multiplicator channels (CEM) with diameter of 10μm. [44]. It can be used to detect particles or radiation with ionizing effect. The principle is illustrated on figure 3.11. Following the two MCP plates there is a phosphor screen which gives a visible picture of the electrons leaving the second MCP. The phosphor screen emits green light ($530-560$nm), and has an afterglow of approximately 2 milliseconds [45]. It works by the same principle as an old monochrome computer screen. The picture from the phosphor screen is captured using a CCD camera and transfered to a computer for further analysis.

To avoid ion feedback[7] the gain of one single MCP has to be kept relatively low, $10^3 - 10^4$, which is barely enough to detect single particles. With two MCP plates (two stage MCP) the total gain can reach 10^7. The channels in a two stage MCP are tilted relatively to each other which also helps in avoiding ion feedback, see figure 3.11c. It should be noted though, that ion feedback is not a great concern at pressures below 10^{-7} mbar [46].

If the gain of the MCP and phosphor screen is kept below the saturation limit, one can assume proportionality between the beam intensity and the light intensity emitted by the phosphor screen.

The two stage MCP is perfect for detecting protons, because the signal from each proton can be seen as single dots on the phosphor screen, see figure 3.12a. It is a bit different for antiprotons, because they annihilate when they hit the detector. The annihilation products are mainly weakly ionising pions and heavily ionising nuclear fragments [47]. These nuclear fragments leave a long trace behind them, see figure 3.12b, which causes deviations from the linear intensity curve. These errors are negligible for high count rates but can become

[7] The large electron density at the exit of a CEM-channel can lead to ionisation of the rest gas. The positive ions will be accelerated back through the channel and lead to new multiplication processes, therefore the name ion feedback [44].
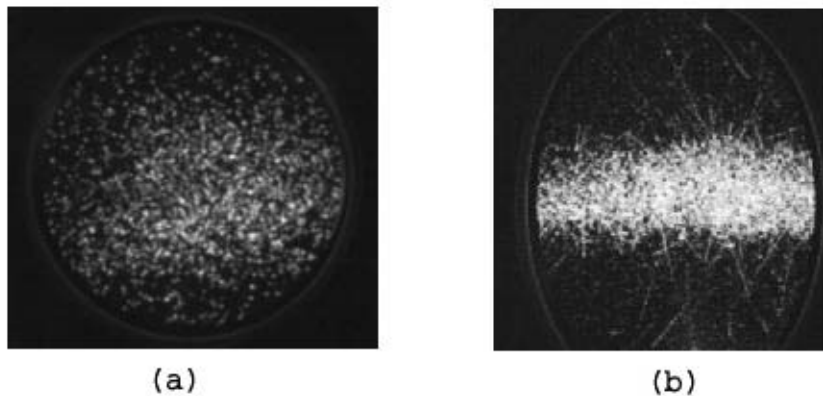
Figure 3.12: Captured image of the phosphor screen when the detector is hit by protons (a) or antiprotons (b). Part of the intensity will come from annihilation products when antiprotons hit the detector.

significant at very low count rates.

We have two detectors in the spectrometer: One between the first analyser and the target, MCP1 on figure 3.9, and one at the exit of the second analyser, MCP2 on figure 3.9. Behind the first detector there is a mirror tilted 45° so that a picture of the phosphor screen can be captured from the side of the apparatus. The first detector is necessary to steer and focus the beam through the target and it can be removed from the beam using a manipulator.

3.4.4 Target

The target is placed between MCP1 and ESA2 (see figure 3.9) and it can be either a set of foils or a gas. To change between foils and gas one has to break the vacuum, but the foil holder can hold three foils at the same time to ensure effective use of beamtime.

The foils are mounted on small stainless steel discs with a 5 or 10 mm aperture, see figure 3.13a. Foils with thicknesses of 400 or 1000 Å are self supporting, while the thinner foils (app. 200 Å) are mounted on a tungsten or nickel mesh with a 90% transmission. Other foils like LiF are mounted on a thin carbon layer.

The gas cell is a 100 mm long cylinder with a diameter of 50 mm, see figure 3.13b. The ends of the gas cell are closed with thin (400-500Å) windows made of carbon or aluminium, so that a relatively high pressure ($> 10^{-5}atm.$) can be maintained in the cell. This is necessary to be able to measure stopping power in gasses [43]. Doing measurements with the gas cell is quite a challenge, because there is a large energy loss and straggling in the windows.

Both the gas cell and the foil holder are isolated from the rest of the spectrometer so that the target foil or gas can be biased with a positive or negative
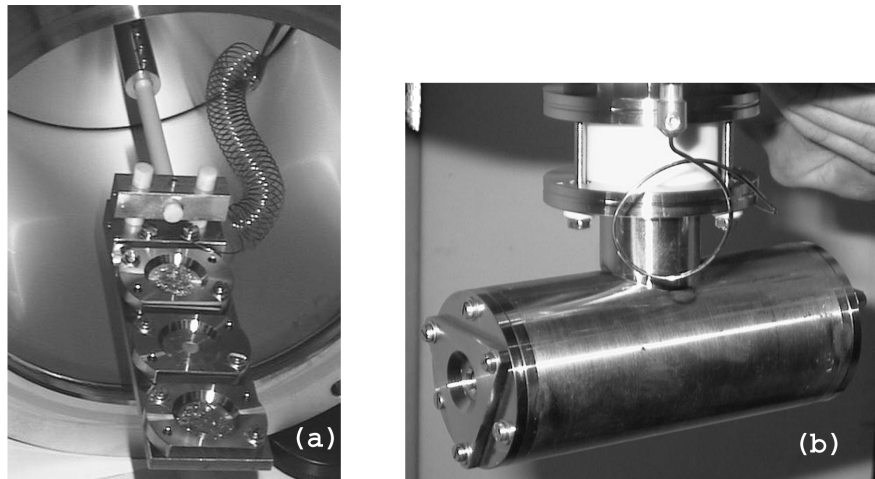
Figure 3.13: The target foil holder (a) with room for three foils, and the gas cell (b).

high voltage. Thus the beam energy at the target can be varied quickly without changing anything at the accelerator/decelerator making measurements over a wide energy range very easy. Another advantage of this technique is that for low energy measurements the beam can be transported through the apparatus at high energies where the emittance is low and the transmission is better. On the other hand, making low energy measurements using high decelerating bias voltages has the disadvantage of reducing the relative energy change of the beam while passing through the target, requiring a large enrgy dispersion. When the relative energy change becomes too small it is no longer possible to separate the decelerated particles from the undecelerated ones. The thin foils mounted on a mesh will always have holes, which is why some particles will pass through the target without loosing any energy.

The gas cell can be applied ± 5 kV, while the foil holder can take up to ± 30 kV. Thus a series of measurements in the range of 1..90 keV can be done by altering the accelerator/decelerator settings only two or three times.

3.4.5   ESA Control System

All the hardware (supplies, camera, valves etc.) are controlled from a single computer equipped with proper A/D, D/A and DIO cards. The computer is then remote controlled from another computer via a network connection. The reason for this is that the apparatus is inaccessible during the measurements with antiprotons (radiation hazard). The control software is described in more details in chapter 4.

Chapter 4

Software

4.1 Hardware Control and User Interface

There were quite many initial requirements for the control software that had to be fulfilled. It should be able to control all the essential hardware like power supplies and detectors and read the status of valves and pumps. It should also acquire the images from the detectors using a CCD camera and be able to manage a sequence of measurements and thereby show and analyse the energy distribution of the particles. In this context the image capturing part should be triggered by the the warning signal from the Antiproton Decelerator and only take a picture when the antiprotons arrive. All this should be hidden behind a nice graphical user interface making operation of the apparatus easy. We also wanted to implement it in a way so that it could be quickly modified by anybody participating in the experiment.

We chose to use LabView from National Instruments [48]. LabView is a visual programming environment designed for rapid prototyping and graphical application development. Furthermore, it integrates hardware access in a very
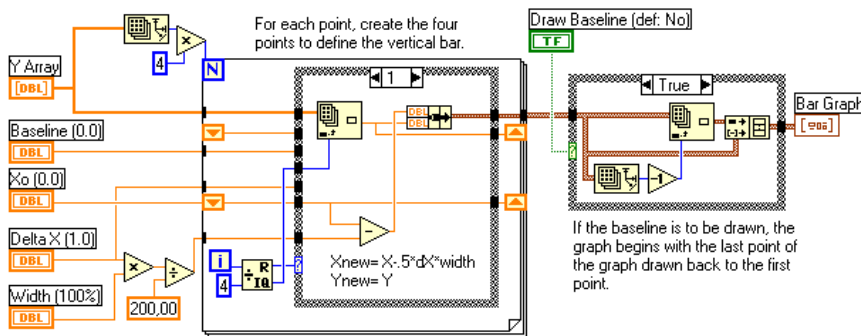
Figure 4.1: An example LabView application. This code actually does the histogramming in the ESA control package.
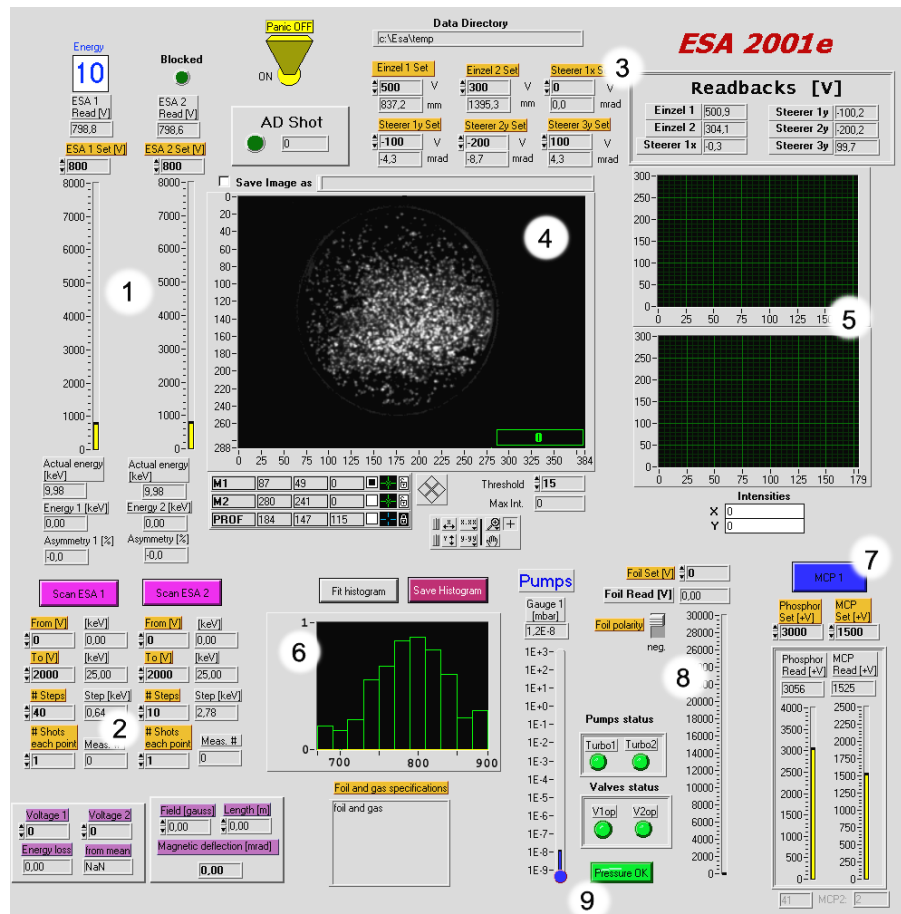
Figure 4.2: Screenshot of the ESA control software.

user friendly way. The programmer does not need any special programming skills in order to create small applications.

The idea behind LabView is more or less the same as in any other programming language: You have a set of primitives like arithmetic types, operators and utility functions which you can put together according to some rules and end up with a program that does exactly what you need. What makes LabView different is that everything including the primitives are small bricks which are wired together in a schematic diagram just like in an electronic design. Some of the bricks eg. numeric indicators or graphs have a visual interface which will appear on the application panel that will make up the graphical user interface.

An example is shown on figure 4.1 which shows the schematic capture of the histogramming module from the ESA control software.

This *wire-the-bricks-together* principle makes LabView very fun and easy to use but for larger application like ours the schematic drawing can easily become a big and confusing mess. To avoid this, parts of the code (schematic drawing) can be organized in separate modules that can be inserted into any other application. This also makes the reuse of existing code easy. This technique is also used in most of the standard modules/bricks that come bundled with the LabView package. These include almost anything desirable from signal processing functions to network protocols.

The initial version of the ESA control software was written during a month and it was mature enough to be used for some measurements and tests with protons. It was able to set and read the power supplies, acquire the image from the camera and even make energy distribution profiles. The camera module was taking pictures of the detector automatically with regular intervals and an AD-trigger signal should still be included in the program. This turned out to be a much bigger problem than we expected, because timing on a microsecond level is very unreliable in a multi tasking operating system like Windows and quite impossible in an environment like LabView[1]. Thus the triggering had to be done on the hardware level which introduced new challenges: Both the camera and the video capture card had external trigger capabilities, but the camera needed an external video timing signal when running in this mode. This problem has been solved by constructing an external trigger module which took the trigger signal from the Antiproton Decelerator as input and supplied the correct trigger and video timing signals for the camera and video capture card.

A picture of the ESA control panel is shown on figure 4.2 with a brief description of the various parts. It has been modified and improved repeatedly during the project lifetime (June 2000 - May 2001) and will probably be improved again before the very last run in June 2002.

4.2   Data Analysis Software

As described in section 5.1, extracting energy loss and straggling from the acquired data is done by fitting Gaussians to histograms. This can be done using almost any graphing software available, but the large amount of data available makes interactive programs quite useless: 1 fit per datapoint, 20 datapoints per foil and 10 foils for both protons and antiprotons add up to 400 fits to be done.

The choice of data analysis software was entirely mine, and I chose to use the ROOT package developed at CERN. ROOT is an object oriented data analysis framework available for free for many operating systems and it has been

---

[1]This is something we have learned the hard way, that is losing precious beam time at CERN.
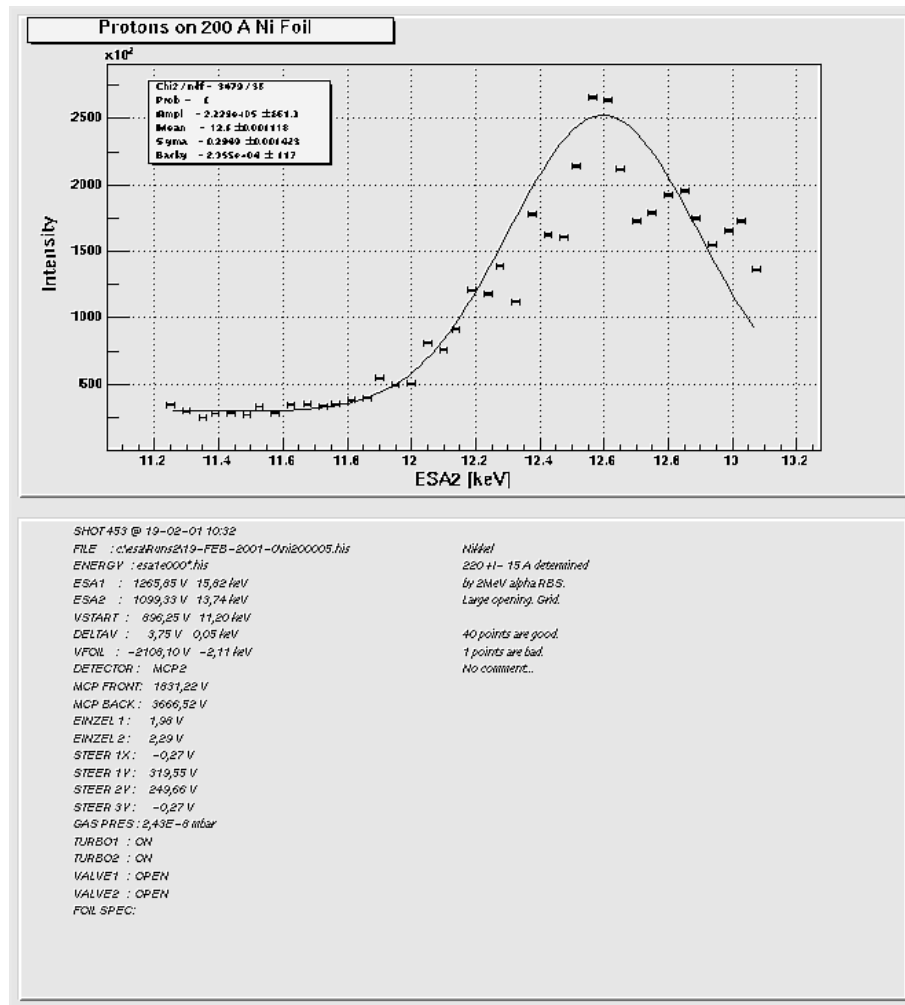
Figure 4.3: Example output produced by the ROOT macro in appendix B.1.

specially designed to handle and analyse large amounts of data in a very efficient way. It has a built-in C/C++ language interpreter which can be used either interactively or to execute previously written scripts. The supplied libraries can be used to organize, visualize and analyse the incoming data or even to build sophistiated graphical user interfaces, see [49] for more details. The drawback of ROOT is that it requires some basic knowledge of either C or C++ programming language, but once that is acquired it can be easily used for both prototyping and large scale applications.

For our data analysis we needed a program that is able to load raw histogram data, fit it to a Gaussian, plot the result and save it together with the data acquisition parameters to a file. For this purpose I have written a small ROOT script that does exactly what is needed and can be executed interactively or unattended. It saves the result in a native ROOT object file and prints it

directly on a printer. An example output is shown on figure 4.3. A listing of the ROOT script is given in appendix B.1.

Chapter 5

Data Taking and Analysis

5.1 Measuring Energy Loss and Straggling

In order to measure energy loss and straggling with the previously described apparatus, we need to know

- the energy distribution of the incoming beam

- the impact energy at the target

- the energy distribution of the particles after passage through the target

- the foil thickness

The energy of the incoming beam is determined by the accelerator/decelerator, however in the case of the RFQD, the antiprotons have an RMS energy spread of almost 10% at the nominal energy of 62 keV and probably increasing when a decelerating ladder voltage is applied[1]. The incoming beam energy is then determined by scanning the first electrostatic analyzer and measuring the beam intensity in the first detector (MCP1 on figure 3.9). The beam intensity is measured by capturing the visible image on the phosphor screen with a CCD camera and integrating the pixel values over a rectangular region which is held constant for a series of measurements. This method gives us only the relative beam intensity which is enough for our purposes.

 With optimal settings the obtained distribution is a gaussian[2] and the beam energy can be extracted as the central value of the distribution (E_0 in future references). To obtain the impact energy at the target we combine the applied target bias, V_{bias}, with the incident energy, E_0. The two values are added in the case of antiprotons and substracted in the case of protons. It should be noted

---

[1]Due to lack of time, we have not measured the RFQ energy spread for other than the nominal energy.

[2]If the detector gain is set too high and the image is saturated, one can end up with the distribution having a flat top which can make things more complicated than just fitting to a gaussian.

that a decelerating bias reaccelerates the particles after leaving the target and vice versa.

After passage through the target, the energy distribution of the particles is determined again using the second analyzer and detector (E_1). This distribution is also approximately a gaussian cf. section 2.7.

Having acquired the quantities mentioned above, the energy loss through the target foil is given by:

$$-\Delta E = E_0 - E_1 \tag{5.1}$$

The stopping power, defined as the differential energy loss per unit length, can be approximated by:

$$-\frac{\mathrm{d}E}{\mathrm{d}x} \approx -\frac{\Delta E}{\Delta x} = \frac{E_0 - E_1}{\Delta x} \tag{5.2}$$

where Δx is the thickness of the target foil. The stopping power is plotted as function of the mean energy of the projectiles through the target

$$E_{mean} = E_0 \pm V_{bias} - \frac{\Delta E}{2} = \frac{E_0 + E_1}{2} \pm V_{bias} \tag{5.3}$$

rather than as a function of the impact energy at the target, $E_0 \pm V_{bias}$. This gives more accurate results, because the projectiles lose their energy gradually through the foil.

One should undoubtly question the validity of equation 5.2. If the energy loss ΔE is small compared to the impact energy at the target, this linear approximation is sufficient, because over small regions any function can be approximated by a linear function. As to the question of how small the energy loss has to be compared to the impact energy, it turns out, that assuming a velocity proportional model for the stopping power, an energy loss of 70% gives a relative error of only 4% (details are given in appendix C). The reference values for stopping power from [2, 8] are believed to be accurate within 10% and also our measurements of the foil thicknesses, Δx, using Rutherford Back Scattering have uncertanities of about 10% (more on that in section 5.2). Therefore an additional error of less than 4% does not make a big difference.

The lithium fluoride foils are mounted on a thin layer of carbon. Hence the measured energy loss through the foils include both the energy loss through carbon and energy loss through lithium fluoride. If the foils are mounted so that the beam first passes the carbon layer, we can extract the stopping power of lithium fluoride by:

$$(\Delta E)_{LiF} \;\; = \;\; (\Delta E)_{total} - (\Delta E)_C \tag{5.4}$$

$$(\Delta E)_C \;\; = \;\; \left(\frac{\mathrm{d}E}{\mathrm{d}x}\right)_C \cdot T_C \tag{5.5}$$

where T_C is the thickness of the carbon layer and $\left(\frac{\mathrm{d}E}{\mathrm{d}x}\right)_C$ is the stopping power of carbon at the energy $E_0 - V_{bias}$ for protons and $E_0 + V_{bias}$ for antiprotons. Also when finding the mean energy through the lithium fluoride layer, one should substract $(\Delta E)_C$ to obtain as accurate energy as possible. The final result

for the stopping power of LiF will include several uncertain parameters like the thicknesses of the carbon and lithium fluoride layers and for the case of antiprotons also the stopping power of carbon.

As described in section 2.7, the energy loss straggling of the particles can be extracted from the scans using the RMS width of the fitted Gaussian:

$$\Omega = \sqrt{\Omega_1^2 - \Omega_0^2} \qquad (5.6)$$

with Ω_0 being the width of the incoming beam and Ω_1 the width of the beam after passage through the target. It should be noted, that the measured straggling is larger than the straggling through an ideal foil due to inhomogenities in the foil thickness cf. section 2.7. These inhomogenities are quite important for the thinnest foils (200Å). For Gaussian foil thickness distributions the measured straggling can be expressed as [27]:

$$\Omega_1 = \sqrt{\Omega_{1,ideal}^2 + \left(\frac{\mathrm{d}E}{\mathrm{d}x}\right)^2 \sigma_x^2} \approx \sqrt{\Omega_{1,ideal}^2 + \delta^2 \Delta E^2} \qquad (5.7)$$

where σ_x is the standard thickness deviation and δ is a foil roughness parameter defined as $\delta = \sigma_x / < x >$.

The applied bias voltage does not only accelerate/decelerate the beam but also acts as an electrostatic lens. As a consequence, a decelerating bias has a defocusing effect and, as the bias increases, fewer and fewer particles pass through the target causing a decreasing transmission. This is illustrated on figure 5.1, where both positive and negative biases have been applied to the target foil during proton measurements.

Furthermore, the applied bias voltage has been found experimentally to have a vertically deflecting effect. Our best guess is that it is caused by the fact, that the electric field from the bias is vertically asymmetric when using the upper or the lower positions on the target foil holder, see figure 3.13a. When using the middle position, these asymmetries are far away from the incoming particles, and the effect is barely noticeable. These side effects do not give much trouble during measurements. In many cases fine tuning of the vertical steerers helps a lot and this extra effort is certainly worth while compared to the aquired bonus of biasing the target (ie. quick variation of impact energy). Usually vertical deflection only becomes a problem when the bias is decelerating and above 50% of the incoming beam energy.

It is obvious that with this method for measuring the energy loss and straggling, we are very sensitive to fluctuations in the incoming beam intensity. The best way to compensate for this is to normalize the measured intensities to the beam intensity at the entrance of the first analyser, ESA1, with some non-destructive diagnostics like a beam transformer. Unfortunately, we do not have such devices in our apparatus and are therefore forced to rely on numbers supplied by "external" devices on the accelerator or decelerator.
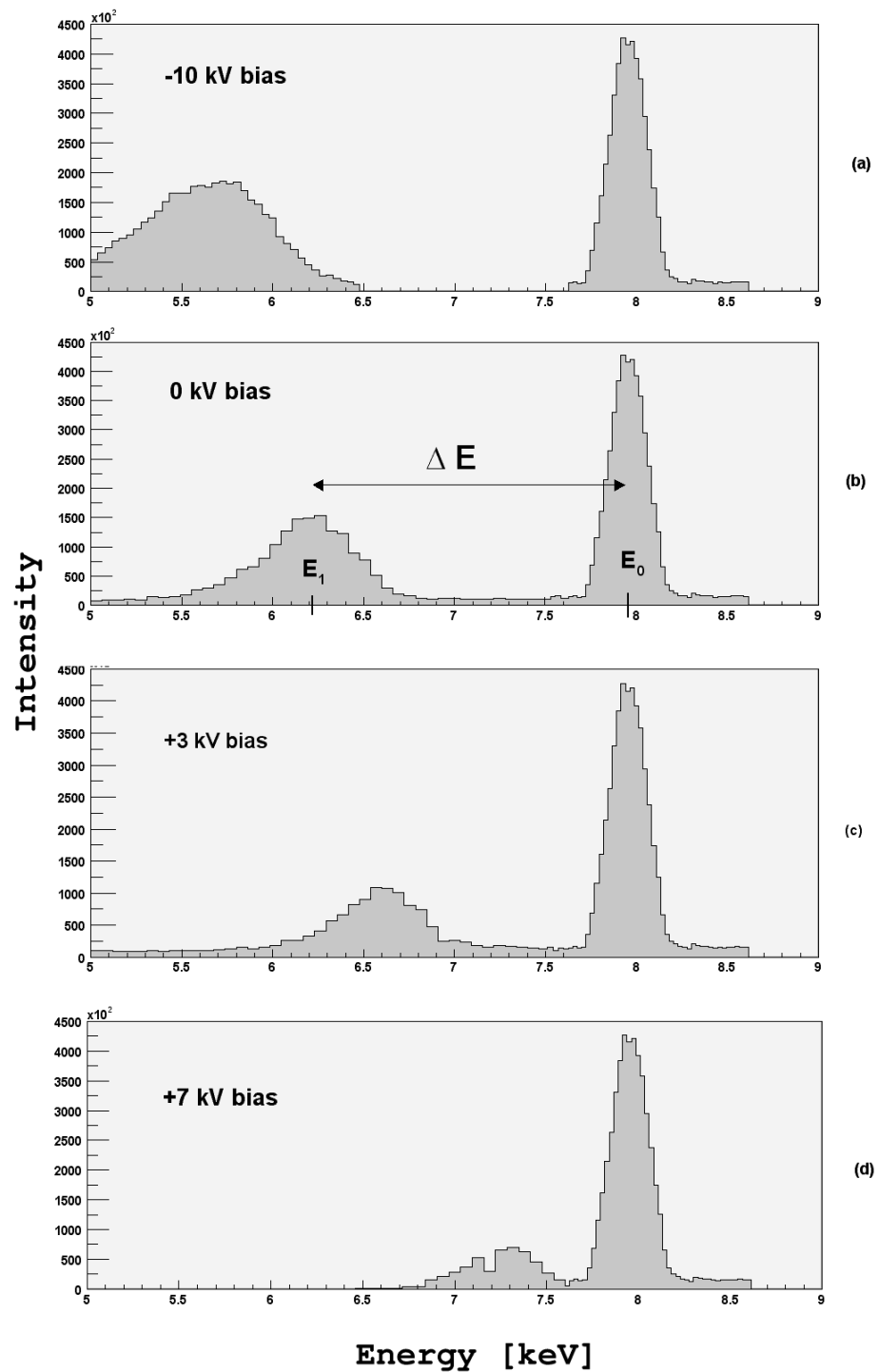
Figure 5.1: Series of measurements showing the energy distributions for protons at various bias voltages. The narrow peak is the energy distribution of the incoming beam while the broad peak is after passage through the target. The figure shows that a negative bias voltage focuses the beam (more particles through the taget) and a positive bias voltage defocuses the beam, because the peak area decreases from (a) to (d). The scans have undergone minor artistic modifications to emphasize the point.

Another way to compensate for intensity fluctuations is to make scans with higher resolution. Thus the number of bins in a histogram can be increased and the shape of the energy distribution can be obtained even for large fluctuations. This workaround works fine with protons where we have a DC beam and can make one step every second, thus completing a scan with 60 steps in one minute. In the case of antiprotons however, we have to wait 2 minutes between each step and making a scan with a resolution of 30 steps (which is not even much for a Gaussian) would require a whole hour!

The obtained data reflect clearly this problem. The proton data was taken with a typical resolution of 30 bins per histogram while the antiproton data was taken with 10 bins per histogram. Consequently there is much more scatter in the antiproton stopping power data than in the proton stopping power data and there is no energy loss straggling data for antiprotons, see chapter 6.

5.2   Measuring the Foil Thickness

The foil thicknesses were measured absolutely using Rutherford back scattering[3] (RBS) with 2 MeV alpha particles. In RBS measurements, the number of particles scattered by an angle (θ, ϕ) within the solid angle $\Delta\Omega$ is given by [50]:

$$\frac{\mathrm{d}n}{\mathrm{d}\Omega}(\theta, \phi) = \frac{N_A \rho x}{4A} \left(\frac{1}{4\pi\varepsilon_0}\right)^2 \left(\frac{2Ze^2}{\mu v^2}\right)^2 \mathrm{cosec}^4 \frac{\theta}{2} \Delta\Omega \qquad (5.8)$$

where ρ is the target density, x the target thickness, μ the reduced mass of target and projectile and v is the velocity of the projectile. Thus the apparatus can be tested by comparing the measured proton stopping powers with the recommended values from [2, 8].

The thickness of the lightest foils like carbon and lithium fluoride can not be measured with this method because of too low signal to noise ratio. For these foils we must rely on the proton stopping power measurements and normalize them to the recomended values to obtain the foil thickness. In any case it is important to check every foil beacuse at such small thicknesses large variations may occur from foil to foil.

---

[3]Rutherford back scattering is described in almost every introductory quantum mechanics or nuclear physics book.

Chapter 6

Results and Discussion

In this chapter I shall present and discuss the results obtained from the energy loss measurements for both protons and antiprotons. The data will be compared to results of the theoretical models and, in some cases, to earlier measurements. The goal was to measure energy loss and energy loss straggling for protons and antiprotons in both noble gas and solid targets with atomic numbers between 1 and 79 down to kinetic energies of a few keV. Due to problems with the gas cell, only solid targets have been measured. These were carbon, aluminium, nickel, gold and lithium-fluoride thus still covering a wide range in atomic numbers and including both metals and insulators.

6.1   Energy Loss in C, Al, Ni and Au

In the case of the aluminium, nickel and gold targets, we were able to determine the foil thicknesses to an accuracy of 10% by the Rutherford Backscattering technique (RBS, see section 5.2). This gives us absolute values of the stopping power for these foils. The RBS technique does not work well for thin targets consisting of light atoms, and hence we were not able to determine the thicknesses of our carbon foils in this way. Instead, we obtained the thickness of our carbon foils via normalization of the measured energy losses of protons to the recommended ICRU curve using a density of 2.0 g/cm^3. Since we used the same carbon foils for both proton and antiproton measurements, we then also obtained values for the stopping power of carbon for antiprotons.

The measured stopping powers of carbon, aluminium, nickel and gold are shown in figures 6.1 and 6.2 as a function of the projectile energy. The proton and antiproton results are plotted on he same graphs to highlight the Barkas effect. Different symbols and colours are used to distinguish between measurements performed at different primary energies and at different times[1].

---

[1] The measurements were done in two runs, which for the case of antiprotons was in November 2000 and again in May 2001. The proton measurements have been done after return from CERN.

For the proton results, we note that for each target material there is good agreement between our experimental data taken with different primary energies and at different times even though there are some minor systematic deviations that might come from the biasing of the target foil (cf. section 3.4). We also notice that there is a nice agreement between our proton data and the recommended ICRU and Andersen-Ziegler[2] curves both with respect to shape and absolute magnitude[3]. This supports the values of the recommended curves, which for these low energies are based on very limited experimental data. These results also provide confirmation of the functionality of the Electrostatic Spectrometer.

A comparison between the proton and antiproton data shows that the Barkas effect at 10 keV is between 40% and 55% of the proton stopping power.

The results of some the recent theoretical models for antiproton stopping are also shown on the graphs. These are the Binary Theory by Sigmund and Schinner (see section 2.6), Sørensen's electron gas model for very low energies (see section 2.5) and a very recent electron gas model by Arista and Lifschitz [51]. For the case of aluminium and gold the results of the quantal harmonic oscillator (see section 2.4) and some previous measurements from LEAR are shown as well. We see that our data is, for the case of gold at least, in very good agreement with the previous measurements that were obtained using completely different techniques [7].

We note that the predictions of Sørensen's electron gas model for very low velocities is in good agreement with our measurements for carbon, gold and nickel, but not for aluminium. However it seems to make a nice extension to the aluminium data from LEAR which in turn is in good agreement with the Binary Theory. Considering the scatter in our data, it might lead us to think that Sørensen's formula is also good for aluminium. Hence this question remains open until further data becomes available.

The results of the Arista-Lifschitz model gives generally too low stopping powers, except for carbon and aluminium above the stopping power maximum, but for carbon we have no data to compare with. For gold it is quite close, but still too low. We should also note, that in the case of nickel and gold, the Arista-Lifschitz prediction fails to merge with the proton curves in the high energy end, where the energy loss can be calculated with high accuracy (e.g. Bethe theory).

Although not in perfect quantitative agreement with our data, the Binary Theory looks most promising. It merges nicely with the proton curve at high energies, where the Barkas term vanishes, and has the correct shape below the stopping power maximum. By correct shape I mean a velocity proportional shape as predicted by the electron gas models and as indicated by our data.

---

[2] No ICRU curve was available for nickel.

[3] For the carbon target, only the shape comparison is meaningful, due to the normalization performed in this case.
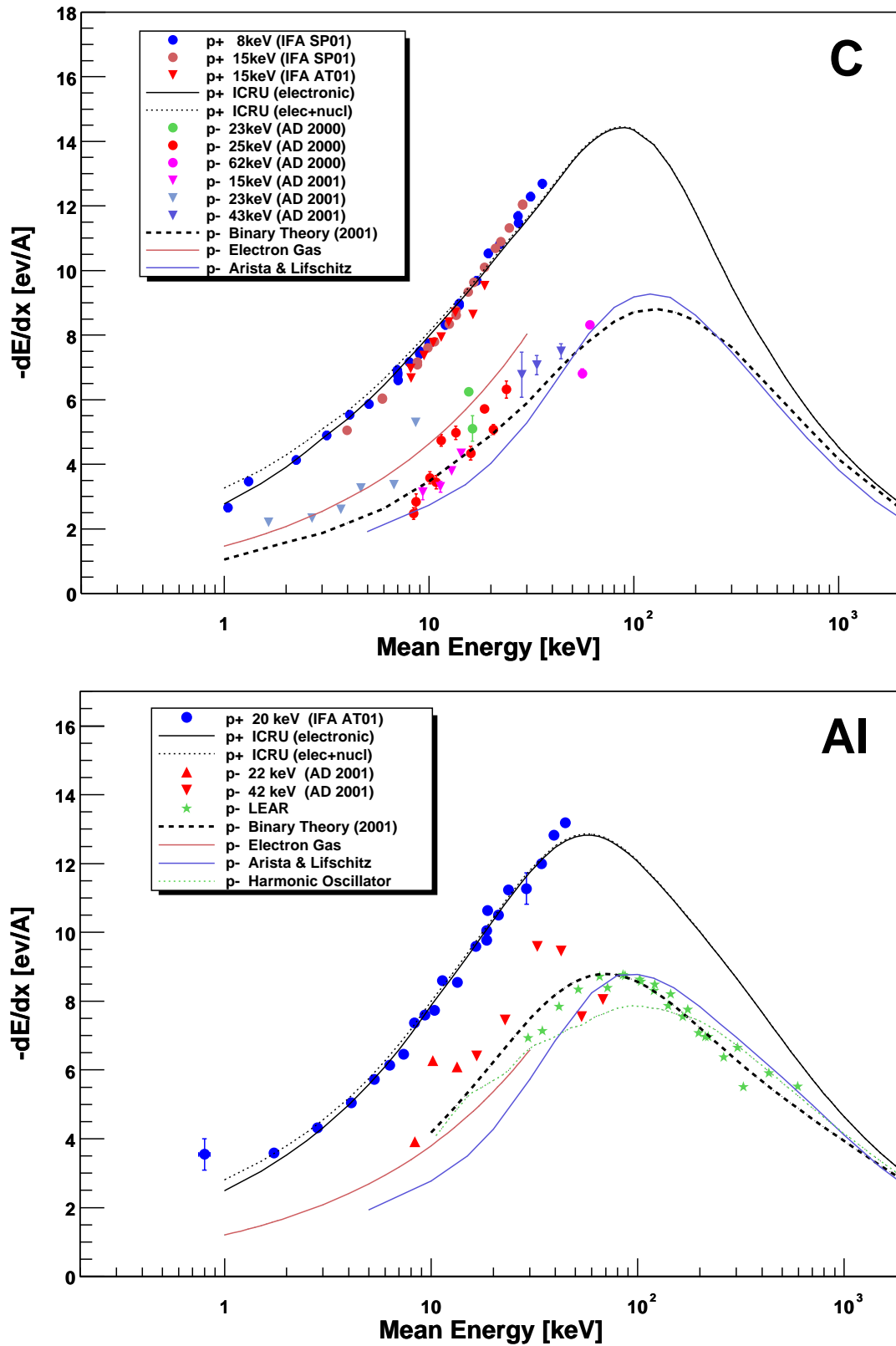
Figure 6.1: Measured stopping powers of carbon and aluminium for protons (p+) and antiprotons (p-). The primary energies for each measurement series are given. Also shown are the ICRU stopping powers for protons [2] and some recent theoretical predictions for antiprotons: Binary Theory [3], Electron Gas by Sørensen [20] and by Arista-Lifschitz [51]. Earlier measurements from LEAR [7] and the results of the quantal harmonic oscillator calculations for aluminium are also plotted.
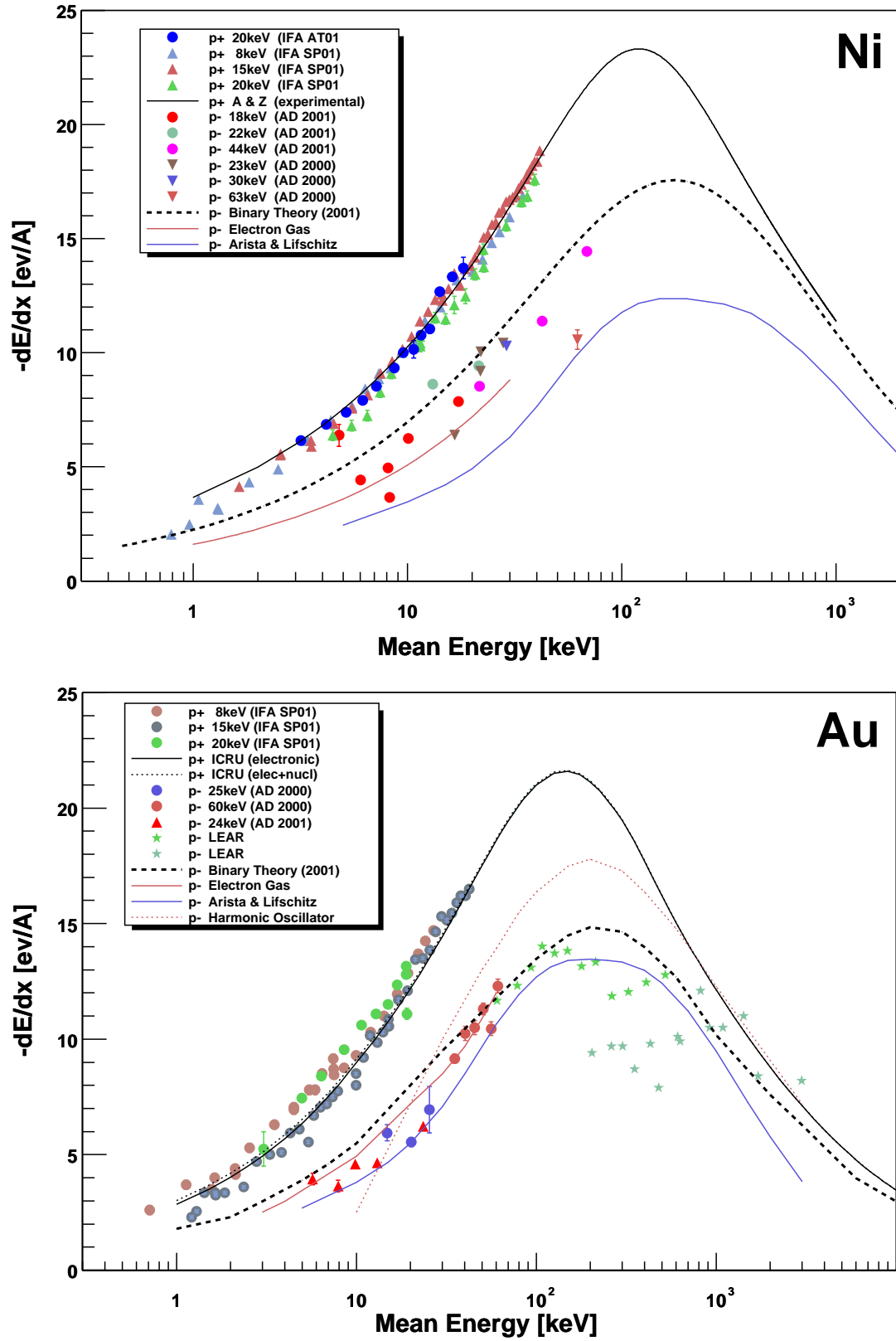
Figure 6.2: Measured stopping powers of nickel and gold for protons (p+) and antiprotons (p-). The primary energies for each measurement series are given. Also shown are the ICRU stopping powers for protons [2] and some recent theoretical predictions for antiprotons: Binary Theory [3], Electron Gas by Sørensen [20] and by Arista-Lifschitz [51]. Earlier measurements from LEAR [7] and the results of the quantal harmonic oscillator calculations for gold are also plotted.
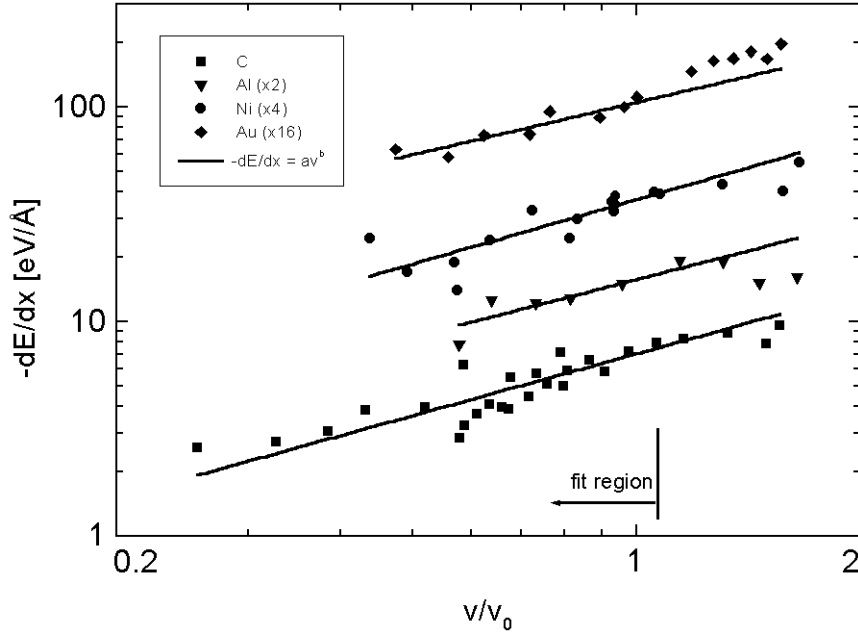
Figure 6.3: Measured antiproton stopping powers as a function of velocity. The solid lines are fits of $-\mathrm{d}E/\mathrm{d}x = av^b$ to the data.

Velocity Proportionality.

As mentioned previously, charge exchange processes like electron capture are expected to contribute significantly to the energy loss of protons, but they are very difficult to treat in the theoretical models. These models predict a velocity proportional stopping at low velocities, which has also been measured with protons for many different targets. So far, significant deviations from velocity proportional stopping of protons have only been observed for noble gas targets [52]. In spite of the agreement in velocity proportional stopping, the proton data can not be used to confirm the validity of the theories, if the theories do not include the charge exchange processes. Charge exchange processes do not exist for antiprotons, hence the stopping power measurements with antiprotons at low energies can indeed be used to evaluate these theories.

Figure 6.3 shows the measured antiproton data for carbon, aluminium, nickel and gold, plotted as a function of the antiproton velocity. The solid lines are functions of the form $-\mathrm{d}E/\mathrm{d}x = av^b$ so that $b = 1$ gives a velocity proportional stopping. The function has been fitted to the antiproton data below 30keV, corresponding approximately to $v \lesssim v_0$, where the free electron gas models should apply. The obtained values for the exponent b are 0.96 ± 0.14 for carbon, 0.89 ± 0.30 for aluminium, 1.00 ± 0.17 for nickel and 0.81 ± 0.14 for gold, all in good agreement with $b = 1$, maybe except for gold where b is slightly lower than 1. Thus we can confirm for the first time that the stopping power of carbon, aluminium, nickel and gold for projectiles which do not take part in charge

exchange processes is velocity proportional at low projectile velocities.

6.2   Energy Loss in LiF

Lithium fluoride is a *large-band-gap* insulator, with an energy gap of approximately 14 eV which is comparable with the minimal excitation energies of the noble gas atoms (e.g. 16 eV for Neon). Hence one would expect a threshold effect in the stopping power, causing large deviations from velocity proportional stopping power, as it has been observed for some noble gasses [52]. Eder et al. [53] have studied the stopping power of several large-band-gap insulators using protons and deuterons as projectiles without finding any deviations from velocity proportional stopping. They explained it by the existence of a bound electron state of a slow proton moving through an insulator, resulting in a local reduction of the band gap. This bound state does however not exist for antiprotons, so deviations from velocity proportionality can still be expected when antiprotons are used as projectiles.

The results of our measurements for LiF are shown on figure 6.4 together with the proton measurements by Eder et al. [53], the recomended proton stopping powers from ICRU [2] and the predictions of the Binary Theory for both protons and antiprotons. We note that the proton measurements by Eder et al. are in very good agreement with the predictions of the Binary Theory but they do not confirm the ICRU values. If we assume that the carbon layer in our foil is 300Å, then our proton measurements agree quite well with the data by Eder et al. and with the Binary Theory for protons. Our antiproton measurements are on the other hand slightly above the predictions of the Binary Theory for antiprotons and close to the proton values from ICRU. If we assume a carbon thickness of 350Å, then the antiproton data come much closer to the predictions of the Binary Theory for antiprotons and our proton data will only lie slightly above the ICRU values (this change in carbon thickness is denoted by the red stars for a few points on figure 6.4). Thus either is the data by Eder et al. and the prediction of the Binary Theory too high or, more likely, the ICRU values for protons and the predictions of the Binary Theory for antiprotons are too low.

It should be noted, that both our proton and antiproton measurements on lithium fluoride were done under very difficult conditions with fluctuating beam intensities. Also considering the uncertanities in the foil thicknesses (cf. section 5.1), a conclusion on this disagreement can not be drawn until further data is available for both protons and antiprotons.

The stopping power of lithium fluoride seems to be somewhat steeper than velocity proportional but not like the v^3 dependence observed for the noble gasses cf. Golser and Semrad [52]. In any case, more accurate data is needed to answer this important question.
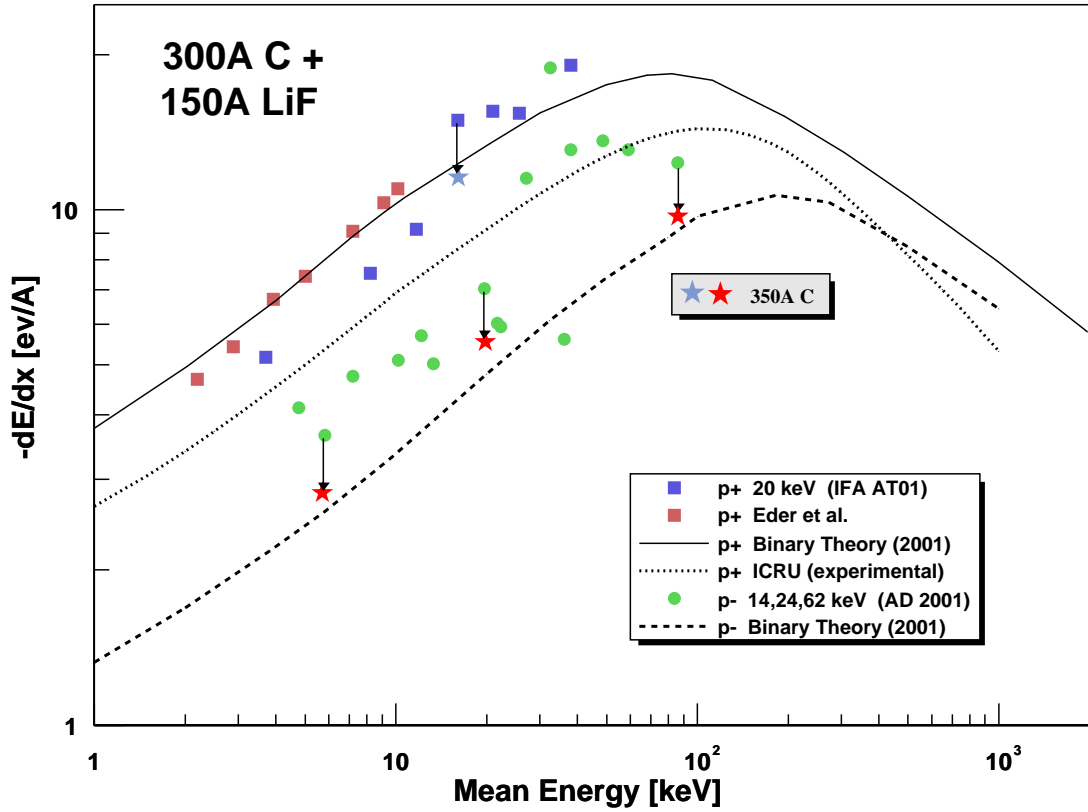
Figure 6.4: Measured stopping power of lithium fluoride. Also shown are some recent proton measurements by Eder et al. [53], the ICRU stopping powers for protons [2] and the Binary Theory for both protons and antiprotons. The stars show the change in stopping power if the thickness of the carbon layer is changed from 300 to 350Å.

6.3   Energy Loss Straggling

As mentioned previously (section 5.1), the energy loss straggling can be obtained from the RMS width, Ω, of the energy distribution of the particles. These values extracted from the carbon, aluminium, nickel and gold measurements with protons are shown on figures 6.5 and 6.6. No straggling data is available for antiprotons due to the low resolution of each scan (see section 5.1). The beam width has been substracted from the fitted values as given by equation 5.6 on page 39. Again we note good agreement between measurements done at different primary energies which ususally cause different beam widths as well. Also shown are the predictions of the electron gas model by Wang and Ma [25] both with and without atomic and texture corrections (as described in section 2.7) and the high velocity asymptote given by the Bohr value (equation 2.28). Recent measurements for carbon made by Konac et al. [54] are also included.

There is in general good agreement between our measurements and the pre-
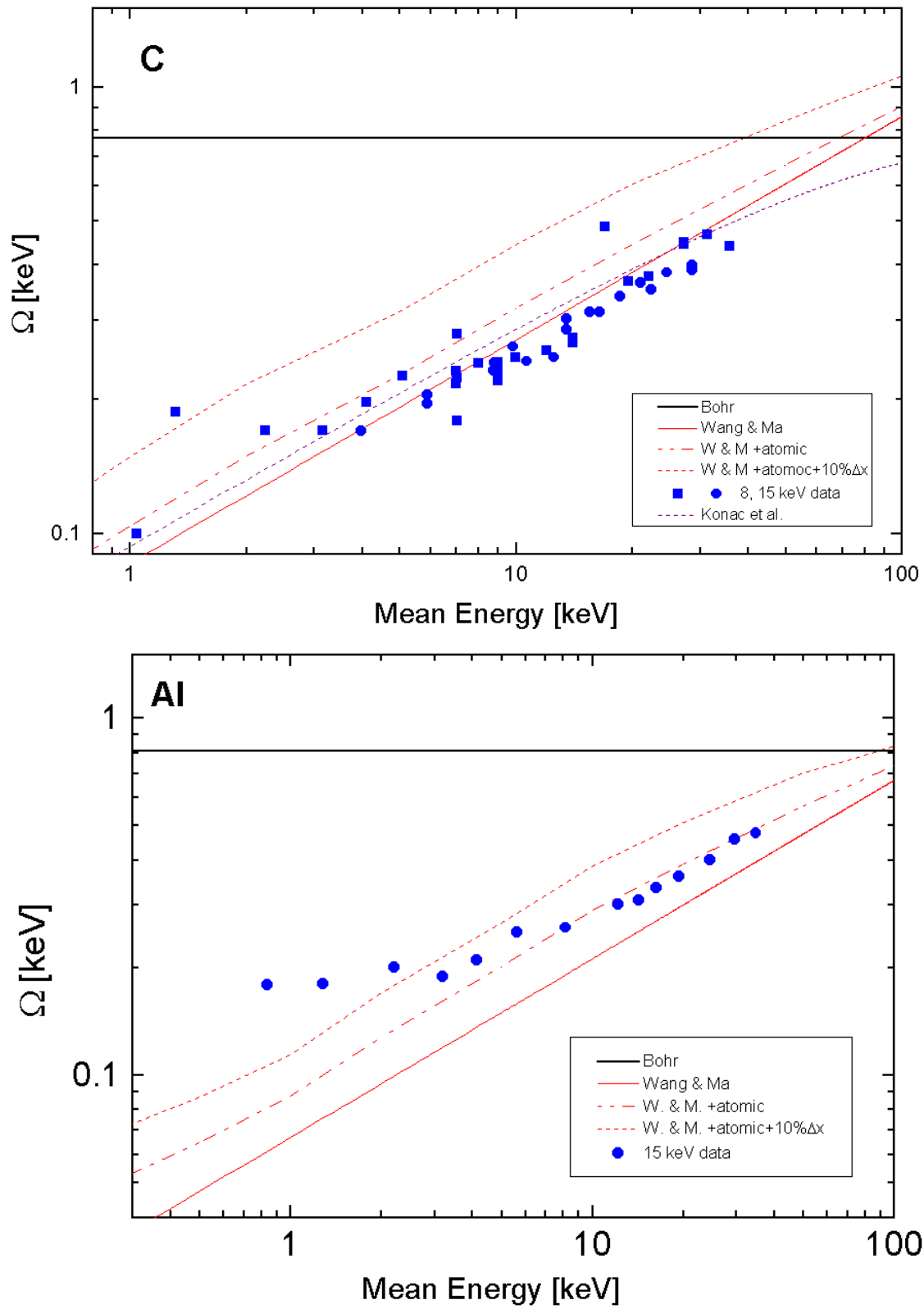
Figure 6.5: Measured energy loss straggling width of protons in carbon and aluminium. Also shown are the predictions of the Wang and Ma [25] electron gas model and this model with added atomic correlation and texture effects. The solid black line is the high energy asymptote (the Bohr value). For carbon, measurements done by Konac et al. [54] are also shown.
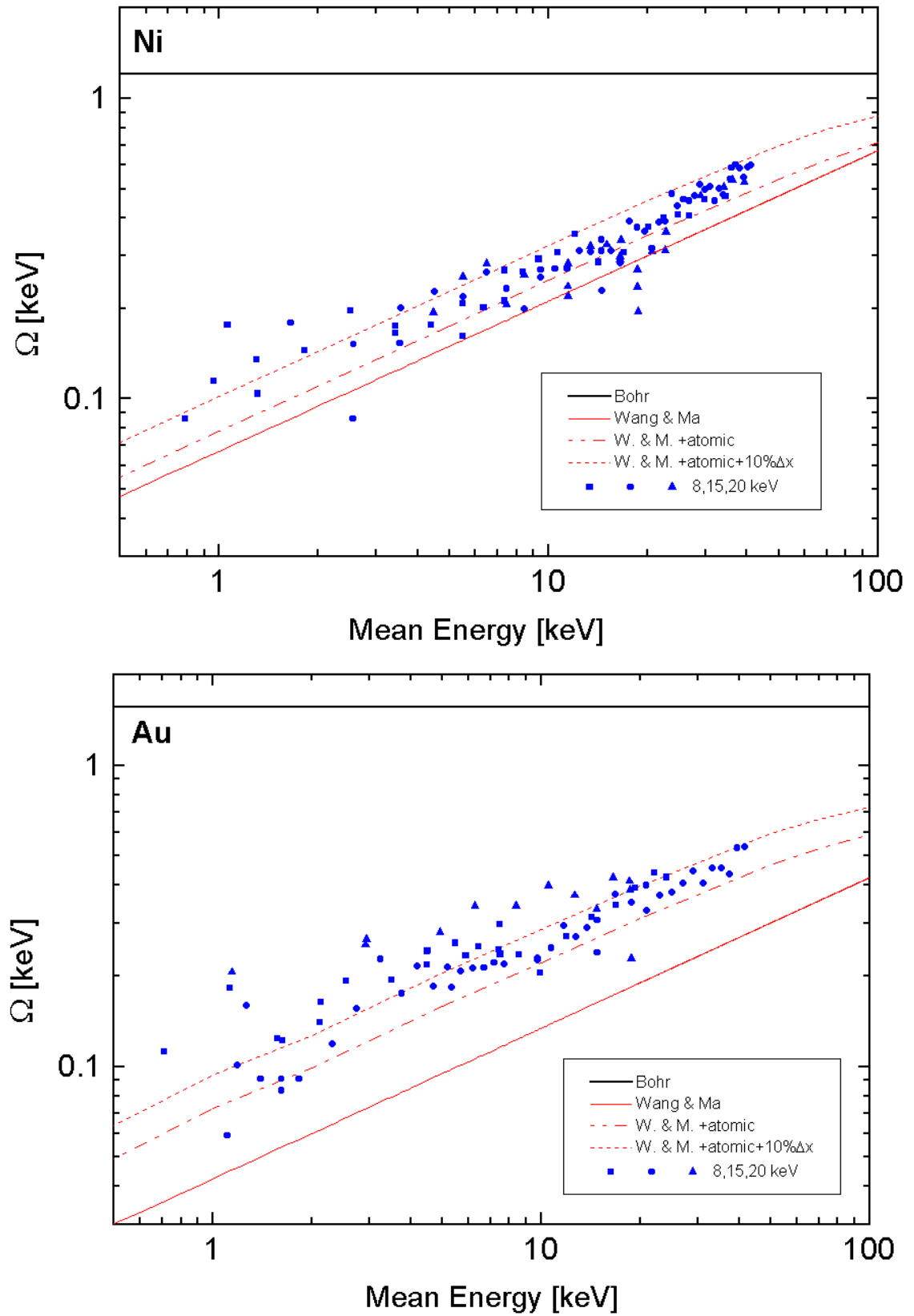
Figure 6.6: Measured energy loss straggling width of protons in nickel and gold. Also shown are the predictions of the Wang and Ma [25] electron gas model and this model with added atomic correlation and texture effects. The solid black line is the high energy asymptote (the Bohr value).

dictions of the Wang-Ma theory except for carbon, where the Wang-Ma formula including the necessary atomic correlation effect gives too high values compared to both our measurements and the measurements by Konac et al.

We note that at the lowest energies of a few keV our data seems to approach a constant value. This could be due to a small error in the measurement of the beam width.

6.4   Antiproton Ranges

To illustrate a simple application of our measurements, we can give a rough estimate of the antiproton ranges using our measurements. For a velocity proportional stopping power we found (cf. equation C.2):

$$\sqrt{E_0} - \sqrt{E_1} = \frac{1}{2}kt \tag{6.1}$$

where E_0 and E_1 is the beam energy before and after the target, k is a constant and t is the target thickness. Because we know the thicknesses of the foils, we can find the value of k from our data:

$$k = \frac{2 \cdot \left(\sqrt{E_0} - \sqrt{E_1}\right)}{t} \tag{6.2}$$

Knowing the value of k, we can find the range of the particles as the thickness, where $E_1 = 0$, that is:

$$R = t\,(E_1 = 0) = \frac{2\sqrt{E_0}}{k} \tag{6.3}$$

These ranges are shown on figure 6.7 for carbon, aluminium, nickel and gold for a few randomly selected points from our energy loss measurements. A k value has been found for each datapoint, and in order to obtain a more descriptive value for k, a function of the form of equation 6.3 has been fitted to the data points. The obtained values for k are shown in table 6.1 for both protons and antiprotons. We may also note, that our "measured" proton ranges are compatible with the values from the compilation of Andersen and Ziegler [8] (these values are not shown on figure 6.7).

Table 6.1: Obtained values for k.

	protons	antiprotons
C	31.5 ± 0.5	12.7 ± 0.7
Al	26.2 ± 0.7	18.2 ± 0.7
Ni	35.6 ± 0.4	20.4 ± 0.8
Au	30.2 ± 0.4	14.2 ± 0.4
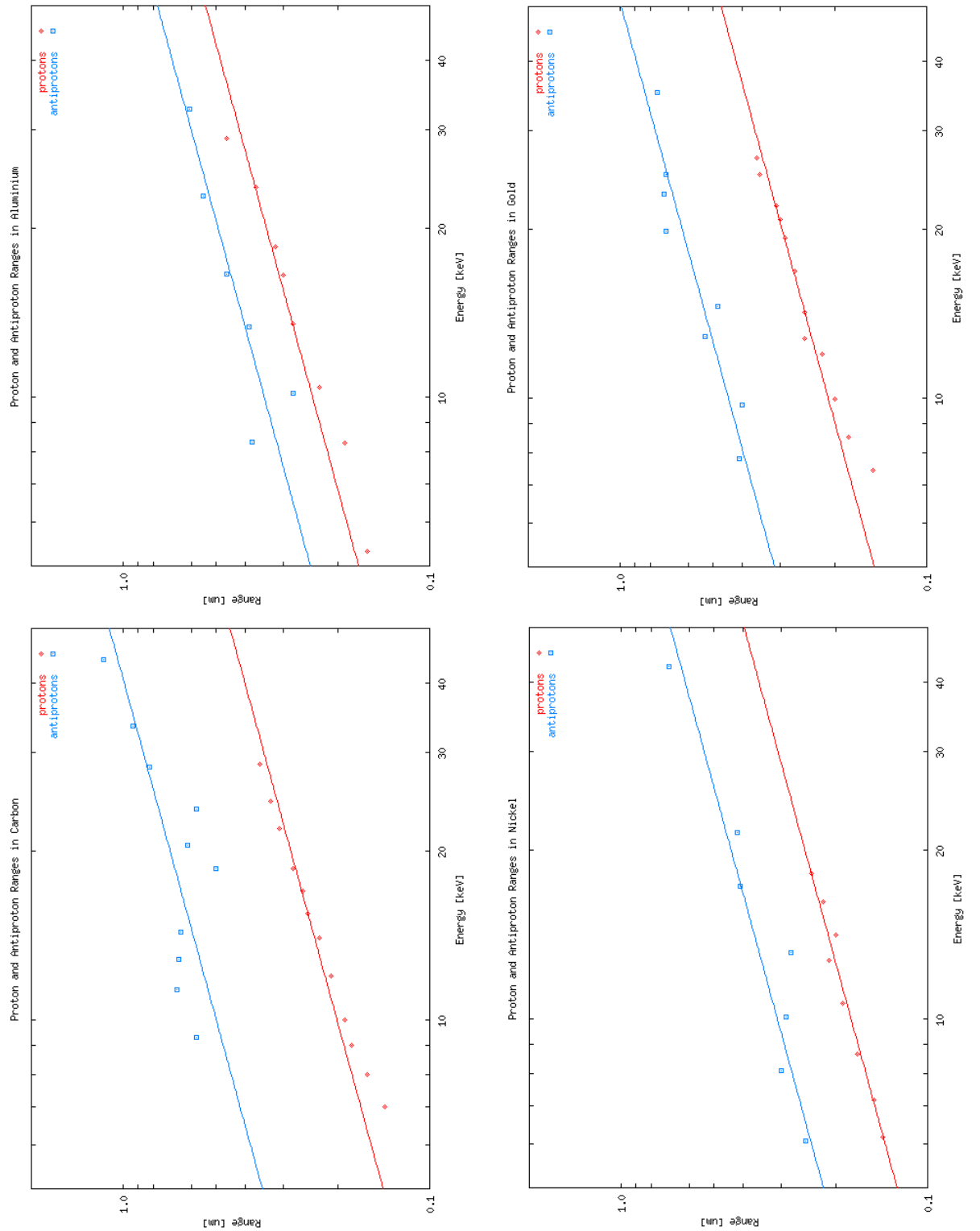
Figure 6.7: Measured proton and antiproton ranges in carbon, aluminium, nickel and gold. The solid lines are fitted functions of the form $y = \frac{2\sqrt{x}}{k}$.

Chapter 7

Summary

The purpose of the experiments described in this thesis has been to measure the stopping power of various materials for protons and antiprotons at energies below the stopping power maximum, where no antiproton measurements have previously been done.

The measurements have been done using an electrostatic spectrometer with the special feature of biasing the target, thus allowing for quick variation of the incoming beam energy. For the proton measurements we have used a simple proton accelerator, whereas the antiproton measurements have been done at the new *Antiproton Decelerator* facility at CERN. Using a newly constructed *Radio Frequency Quadrupole Decelerator* as post-AD decelerator, antiprotons with variable kinetic energy between 0 and 120 keV were available.

The stopping power of five different solid targets have been succesfully measured in the energy range of 1-40 keV for protons and approximately 2-90 keV for antiprotons with the actual limits varying for each target. The targets were carbon, aluminium, nickel, gold and lithium fluoride, covering a range between 6 and 79 in atomic numbers and including a large-band-gap insulator (LiF). The thicknesses of the aluminium, nickel and gold foils have been determined using Rutherford back scattering, thus giving us absolute values of the stopping power of these foils. For carbon and lithium fluoride, the thicknesses had to be estimated by normalization to previous measurements giving us only relative values of the stopping power.

For carbon, aluminium, nickel and gold it has been found, that the antiproton stopping powers below 30 keV are velocity proportional as predicted by several theoretical models. This is the first time that velocity proportional stopping power can be reported for particles which do not take part in charge exchange processes. Furthermore, a quantitative comparison between these data and the predictions of recent theoretical models has shown, that the Binary Theory by Sigmund and Schinner gives good estimates of the antiproton stopping powers below the stopping power maximum. Sørensen's electron gas formula for low energy antiproton stopping has also been found to be in good quantita-

tive agreement for these targets with the possible exception of aluminium, for which data only above 8 keV is available. The electron gas model by Arista and Lifschitz has been found to give too low estimates below the stopping power maximum.

The proton measurements for carbon, aluminium, nickel and gold have been compared to the recomended proton curves by ICRU, or proton curves by Andersen and Ziegler (nickel), and good agreement has been found over the entire measured energy range. Furthermore, energy loss straggling data has been extracted from the proton measurements and compared to the Wang-Ma electron gas calculations. It has been found, that the Wang-Ma calculations give good estimates of the straggling for slow protons in aluminium, nickel and gold, if the atomic correlation and the target inhomogenety corrections are added. For carbon, the Wang-Ma calculations overestimate the energy loss straggling, both if compared to our measurements and if compared to measurements done previously by Konac et al.

A comparison between the proton and antiproton data has shown that the Barkas effect at 10 keV is between 40% and 55% of the proton stopping power.

Due to large uncertainities in our lithium fluoride measurements, we have not been able to determine whether the stopping power of lithium fluoride for antiprotons is velocity proportional or not. The Barkas effect in lithium fluoride at a projectile energy of 10 keV has been found to be approximately 50% of the proton stopping power predicted by the Binary Theory and measured by Eder et al. The recomended values from ICRU for protons in lithium fluoride have been found to be too low compared to these measurements. We have not been able to draw a conclusion in this disagreement, because our relative measurements for lithium fluoride had to be normalized to some other reference.

To illustrate the applicability of our measurements, rough estimates of proton and antiproton ranges in carbon, aluminium, nickel and gold have been calculated.

As for the future experiments, it is important to obtain accurate and, if possible, absolute measurements of the stopping power of lithium fluoride for both protons and antiprotons. Also antiproton stopping power measurements for other targets, in particular for noble gasses, would be desirable. It would also be interesting to compare the energy loss straggling of protons with that of antiprotons, but this can only be obtained at the expense of valuable beam time.

Appendix A

Characteristics

A.1 Antiproton Decelerator

Table A.1: AD Beam Characteristics at 100 MeV/c [34].

	Obtained	**Design**	**Unit**
Acceptance hor./ver. at 3.5 GeV/c	180π / 200π	200π / 200π	mm·mrad
Momentum	100	100	MeV/c
Intensity	2×10^7	1.2×10^7	$\overline{p}$
Period	1.9	1.0	sec
Emittance (87% beam) ϵ_h/ϵ_v $\Delta p/p$ debunched $\Delta p/p$ bunched	$1\pi/1\pi$ 1×10^{-4} 2×10^{-3}	$1\pi/1\pi$ 1×10^{-4} 1×10^{-3}	mm·mrad
Bunch length (minimum)	230 - 390	200 - 500	nsec

Table A.2: Beam cooling at different energies [34].

Momentum	**Cooling**	**Final emittance (87% beam)**						**Duration**	
		Obtained			Design			Obtained	Design
[GeV/c]		ϵ_h	ϵ_v	$\Delta p/p$	ϵ_h	ϵ_v	$\Delta p/p$	[sec]	
		[mm·mrad]		[%]	[mm·mrad]		[%]		
3.5	Stochastic	3π	4π	3.5	5π	5π	0.1	20	20
2.0	Stochastic	3π	3.5π	0.08	5π	5π	0.03	15	15
0.3	Electron	5π	2π	0.05	2π	2π	0.1	16	6
0.1	Electron	1π	2π	0.01	1π	1π	0.01	10	1

A.2   RFQ decelerator

Table A.3: Some Parametres of the CERN RFQD [40].

Parameter	Value
RF frequency	202.5 MHz
Impedance	13.8 kΩ
Electrode voltage	167 kV
Max. electric field	33 MV/m
Dissipated power	1.1 MW
Min. aperture radius	0.4 cm
Max. vane modulation	2.9
Input energy	5.314 MeV
Output energy (RFQD) ± DC bias	63 keV ± 60 keV
Transverse acceptance	15π mm.mrad
Phase/energy acceptance	$\pm 10°$ / $\pm 0.9 \times 10^{-3}$
Decceleration efficiency (theoretical)	45%
RMS energy spread at 62 keV (measured with ESA)	5.7 ± 0.5 keV

A.3   Electrostatic Spectrometer

Table A.4: Chosen Parametres for the Spectrometer [43].

Par.	Description	Value	Constrains
E_{kin}	Beam energy	0..120 keV	Determined by the RFQD
d	Distance between electrodes	20 mm	18 mm beam diameter.
h	Height of electrodes	60 mm	$d \ll h < 150$ mm
ϕ	Bending angle	90°	Maximum dispersion
L	Bending length	392.7 mm	$L > 157$ mm
ΔV	Potential difference	0-16 kV	$\Delta V/d = 2E_{kin}/eR$
R	Bending radius	250 mm	$R > 200$ mm
L_a	Drift length after ESA2	250 mm	$L_c = 2R^2/L_b$, $\phi = 90°$
L_b	Distance between ESA1 and ESA2	500 mm	$L_b > 2d_j + L_g$
L_c	Drift length before ESA1	500 mm	$L_c = 2R^2/L_b$, $\phi = 90°$
d_j	Distance from ESA to aperture	15 mm	$d_j > \Delta V/2kV \cdot 1mm$

Appendix B

Software Listings

B.1 ROOT Macro for Fitting Histograms

```
void pbarfit ( char *title, Int_t n,
               char *dat2, char *par2,
               char *foil, char *info )
{
        /* Root C++ macro to analyze ESA-pbar measurements.
           Load .par2 and .dat2 files, fit and display them nicely.
           When the script is finished, you can change the look of the
           graph, and save it manually.

           January 2001, Alexandru Csete
        */

        gROOT→Reset (); // Reset environment
        gStyle→SetOptFit (1111); // Show Fit results (see manual)

        FILE *fp = fopen (dat2,"r");

        char line[81];
        char pload[20],pign[20]; // string to display points loaded and ignored
        Int_t i=0, ip=0;
        Float_t x[n],ex[n],y[n],ey[n];

        /* Read the data file */
        while (fgets (&line, 81, fp) ) {
                if (line[0] != '#') {
                        sscanf (&line[0], "%f%f", &x[i], &y[i]);
                        x[i] *= 0.0125;
                        ex[i] = x[i]*0.003; // hor. error
                        ey[i] = 5*sqrt(y[i]); // ver. error
                        printf ("x=%8.2f, ex=%8.2f, y=%8.2f, ey=%8.2f\n",
```

```
                                     x[i], ex[i], y[i], ey[i]);
                         i++;
                    }
               else ip++;
          }
     fclose (fp);
     sprintf (pload, "%d points are good.", i);
     sprintf (pign, "%d points are bad.", ip);

     /* Create the canvas */
     canv = new TCanvas ("canv", "ESA", 700, 800);
     canv→SetFillColor (18);
     canv→GetFrame()→SetFillColor(19);
     canv→GetFrame()→SetBorderSize(12);
     canv→Divide(1,2);
     canv→cd(1);
     canv_1→SetGrid();

     /* Create the graph */
     gr = new TGraphErrors (i, x, y, ex, ey);
     gr→SetTitle (title);
     gr→SetMarkerColor (4);
     gr→SetMarkerStyle (7);
     gr→Draw ("AP");
     canv→Update ();
     gr→GetXaxis()→SetTitle ("ESA2 [keV]");
     gr→GetXaxis()→CenterTitle();
     gr→GetXaxis()→SetLabelSize(0.03);
     gr→GetYaxis()→SetTitle("Intensity");
     gr→GetYaxis()→CenterTitle();
     gr→GetYaxis()→SetLabelSize(0.03);
     gr→Draw ("AP");
     canv→Update();

     /* Create a gaussian with background */
     TF1 *bgaus = new TF1 ("bgaus",
"[0]*exp(-0.5*((x-[1])/[2])**2)+[3]",
                              x[0], x[i-1]);
     /* Estimate the parameters */
     bgaus→SetParNames ("Ampl", "Mean", "Sigma", "Backg");
     bgaus→SetParameters (y[i/2], x[i/2], 0.2, y[0]);

     bgaus→SetLineWidth (1);
     bgaus→SetLineColor (1);

     /* Set parameter limits if data is "ugly" */
     /* bgaus->SetParLimits(0,0,2e5); */
```

```
        bgaus->SetParLimits(1,18.5,18.55);
        bgaus->SetParLimits(2,0.1,0.2);
        bgaus->SetParLimits(3,3.8e5,4.1e5);
*/

/* Fit the gaussian */
gr→Fit ("bgaus","");

canv→cd (2);
canv_2→Range (0, 0, 80, 28);

/* ESA Parameter info */
fp = fopen (par2, "r");
TText t (0, 0, "a");
t.SetTextFont (50);
t.SetTextSize (0.022);
t.SetTextColor (12);
i=27;
while (fgets (&line, 81, fp) )
        t.DrawText (5, 7+0. 7*i− −, line);
fclose (fp);

/* Foil info */
fp = fopen (foil, "r");
i = 26;
while (fgets (&line, 81, fp) )
t.DrawText (50, i− −, line);
fclose (fp);

t.DrawText (50, − −i, pload);
t.DrawText (50, − −i, pign);

/* Additional info */
fp = fopen (info, "r");
while (fgets (&line, 81, fp) ) {
        t.DrawText(50,− −i,line);
}
fclose (fp);
/* Update the canvas and bail out */
canv_2→Modified ();
canv_2→Update ();
canv→cd ();
}
```

Appendix C

Validity of $\mathrm{d}E/\mathrm{d}x \approx \Delta E/\Delta x$ for Velocity Proportional Models

Let us consider a velocity proportional model for the stopping power:

$$-\frac{\mathrm{d}E}{\mathrm{d}x} = k\sqrt{E} \qquad \text{(C.1)}$$

where k is a constant. We wish to investigate the validity of equation 5.2, that is:

$$-\frac{\mathrm{d}E}{\mathrm{d}x} \approx -\frac{\Delta E}{\Delta x} = \frac{E_0 - E_1}{t}$$

where E_0 is the incoming beam energy and E_1 is the beam energy after passage through the target of thickness t. By integrating equation C.1 we obtain:

$$
\begin{aligned}
-\int_{E_0}^{E_1} \frac{1}{\sqrt{E}}\mathrm{d}E &= \int_0^t k\mathrm{d}x \\
\sqrt{E_0} - \sqrt{E_1} &= \frac{1}{2}kt \qquad\qquad \text{(C.2)}
\end{aligned}
$$

Lets say, that we plot a data point using $-\frac{\mathrm{d}E}{\mathrm{d}x} = \frac{E_0 - E_1}{t}$ and because of this, the point will be misplaced with an error ε as shown on the figure above. The

65
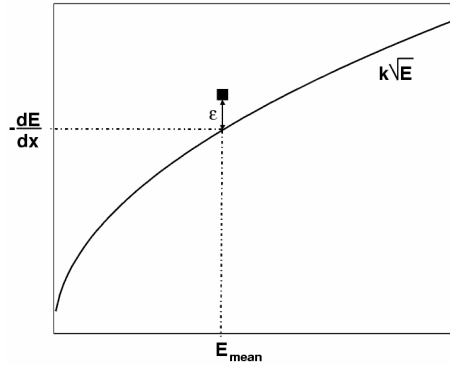
relative error, ε_{rel}, is then given by:

$$
\begin{aligned}
\varepsilon_{rel} \quad &= \quad \frac{\frac{E_0 - E_1}{t} - k\sqrt{E}}{k\sqrt{E}} \\
&= \quad \frac{E_0 - E_1 - kt\sqrt{E}}{kt\sqrt{E}} \\
&= \quad \frac{E_0 - E_1}{kt\sqrt{E}} - 1
\end{aligned} \tag{C.3}
$$

Inserting equation C.2 into equation C.3 we obtain:

$$
\varepsilon_{rel} = \frac{E_0 - E_1}{2\left(\sqrt{E_0} - \sqrt{E_1}\right)\sqrt{E}} - 1 \tag{C.4}
$$

If we use the mean energy of the projectiles through the target, $E = \frac{E_0 + E_1}{2}$, the above equation becomes:

$$
\begin{aligned}
\varepsilon_{rel} \quad &= \quad \frac{E_0 - E_1}{2\left(\sqrt{E_0} - \sqrt{E_1}\right)\sqrt{\frac{E_0 + E_1}{2}}} - 1 \\
&= \quad \frac{1 - \frac{E_1}{E_0}}{\sqrt{2}\left(1 - \sqrt{\frac{E_1}{E_0}}\right)\sqrt{1 - \frac{E_1}{E_0}}} - 1
\end{aligned} \tag{C.5}
$$

At this point it is convenient to introduce the dimensionless constant $\beta = E_1/E_0$ with which we get:

$$
\begin{aligned}
\varepsilon_{rel} \quad &= \quad \frac{1 - \beta}{\sqrt{2}\left(1 - \sqrt{\beta}\right)\sqrt{1 - \beta}} - 1 \\
&= \quad \frac{1}{\sqrt{2}}\frac{1 + \sqrt{\beta}}{\sqrt{1 + \beta}} - 1
\end{aligned} \tag{C.6}
$$

This equation is plottet on figure C.1 and the result is somewhat surprising. Even for an energy loss of 75% of the incoming beam energy the relative error is not more than 5%.

It is tempting to try the same calculation with energies other than the mean energy of the projectiles through the target. If we use $E = E_0$ the relative error becomes:

$$
\varepsilon_{rel} = \frac{1}{2}\sqrt{\beta} - \frac{1}{2} \tag{C.7}
$$

This equation is plotted on figure C.2 and we see that this error is quite larger than if we use the mean energy.
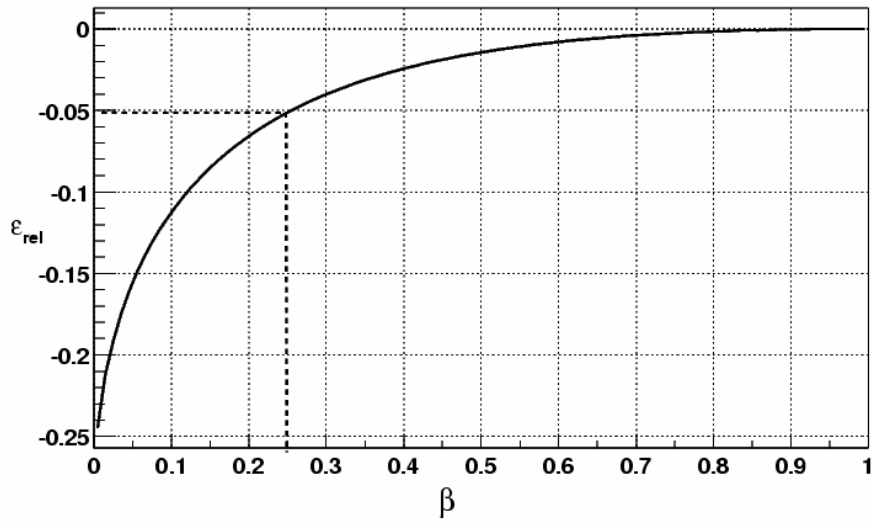
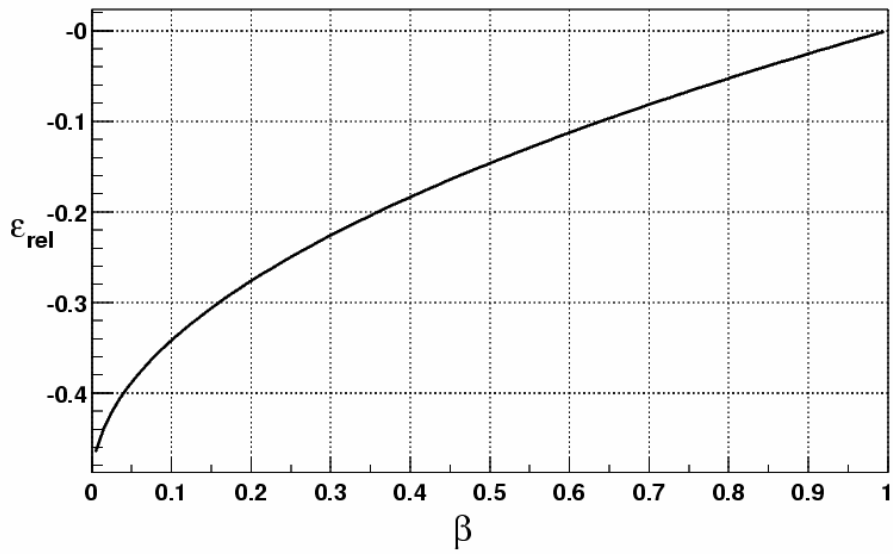Figure C.1: The relative error as a function of β for $E = \frac{E_0 + E_1}{2}$.

Figure C.2: The relative error as a function of β for $E = E_0$.

Bibliography

[1] Niels Bohr, Phil- Mag. **25** (1913) 10.

[2] ICRU Report 49, *Stopping Powers and Ranges for Protons and Alpha Particles*, 0-913394-47-5, 1993

[3] P. Sigmund and A. Schinner, *Binary Theory of Antiproton Stopping*, Eur. Phys. J. **D15**, 165-172 (2001).

[4] W. H. Barkas, J. N. Dyer and H. H. Heckman, *Resolution of the Σ^{-}-Mass Anomaly*, Phys. Rev. Lett. **11** (1963) 26. See also p. 138 for errata.

[5] L. H. Andersen, P. Hvelplund, H. Knudsen, S. P. Møller, J. O. P. Pedersen, E. Uggerhøj, K. Elsener and E. Morenzoni, *Measurement of the Z_1^3 Contribution to the Stopping Power Using MeV Protons and Antiprotons: The Barkas Effect*, Phys. Rev. Lett. **62** (1989) 1731.

[6] R. Medenwaldt, S. P. Møller, E. Uggerhøj, T. Worm, P. Hvelplund, H. Knudsen, K. Elsener and E. Morenzoni, *Measurement of the Stopping Power of Silicon for Antiprotons Between 0.2 and 3 MeV*, Nucl. Instrum. Methods **B58** (1991) 1.

[7] S. P. Møller, E. Uggerhøj, H. Bluhme, H. Knudsen, U. Mikkelsen, K. Paludan and E. Morenzoni, *Direct Measurements of the Stopping Power for Antiprotons of Light and Heavy Targets*, Phys. REv. **A56** (1997) 2930.
S. P. Møller, E. Uggerhøj, H. Bluhme, H. Knudsen, U. Mikkelsen, K. Paludan and E. Morenzoni, *Measurement of the Barkas Effect Around the Stopping-Power Maximum for Light and Heavy Targets*, Nucl. Instrum. Methods **B122** (1997) 162.

[8] H. H. Andersen and J. F. Ziegler, *Hydrogen Stopping Powers and Ranges in All Elements*, Pergamon Press, Elmsford, New York.

[9] http://www.srim.org/

[10] Ejvind Bonderup, *Penetration of Charged Particles Through Matter*, Lecture Notes, Institute of Physics and Astronomy, University of Aarhus, 1981.

[11] Søren Pape Møller, *Ph.D. Thesis*, Institute for Storage Ring Facilities, University of Aarhus, 1998.

[12] J. C. Ashley, R. H. Ritchie and W. Brandt, Z_1^3 *Effect in the Stopping Power of Matter for Charged Particles*, Phys. Rev. **B5** (1972) 2393.

[13] J. C. Ashley, R. H. Ritchie and W. Brandt, Z_1^3-*Dependent Stopping Power and Range Contributions*, Phys. Rev. **A8** (1973) 2402.

[14] J. D. Jackson and R. L. McCarthy, z^3 *Corrections to Energy Loss and Range*, Phys. Rev. **B6** (1972) 4131.

[15] J. Lindhard, *The Barkas Effect - or Z_1^3, Z_1^4 Contributions to the Stopping of Swift Charged Particles*, Nucl. Instrum. Methods **132** (1976) 1.

[16] P. Sigmund and U. Haagerup, *Bethe Stopping THeory for a Harmonic Oscillator and Bohr's Oscillator Model of Electronic Stopping*, Phys. Rev. **A34** (1986) 892.

[17] H. H. Mikkelsen and P. Sigmund, *Barkas Effect in Electronic Stopping Power: Rigorous Evaluation for the Harmonic Oscillator*, Phys. Rev. **A40** (1989) 101.

[18] H. H. Mikkelsen and H. Flyvbjerg, *Exact Stopping Cross Section of the Quantum Harminoc Oscillator for a Penettrating Point Charge of Arbitrary Strength*, Phys. Rev. **A45** (1992) 3025.

[19] J. Lindhard and M. Scharff, *Energy Dissipation by Ions in the kev Region*, Phys. Rev. **124** (1961) 128.

[20] A. H. Sørensen, *Barkas Effect at Low Velocities*, Nucl. Intrum. Methods **B48** (1990) 10.

[21] P. Sigmund and A. Schinner, *Binary Stopping Theory for Swift Heavy Ions*, Eur. Phys. J. **D12**, 425-434 (2000).

[22] P. Sigmund and A. Schinner, *Binary Theory of Light-Ion Stopping*, Preprint submitted to NIMB.

[23] J. Lindhard and M. Scharff, Mat. Fys. Medd. Dan. Vid. Selsk. **27** No. 15 (1953).

[24] E. Bonderup and P. Hvelplund, *Stopping Power and Energy Straggling for Swift Protons*, Phys. Rev. **A4** (1971) 562.

[25] Y. N. Wang and T. C. Ma, *Stopping Power and Energy Loss Straggling of Slow Protons in a Strongly Coupled Degenerate Electron Gas*, Nucl. Instrum. Methods **B51** (1990) 216.

[26] Neil W. Aschroft and N. D. Mermin, *Solid State Physics*, Saunders Colelge Publishing, 1976.

[27] F. Besenbacher, J. U. Andresen and E. Bonderup, *Straggling in Energy Loss of Energetic Hydrogen and Helium Ions*, Nucl. Instr. Methods, **168** (1980) 1.

[28] T. Azuma et al., *Atomic Spectroscopy and Collisions Using Slow Antiprotons*, CERN/SPSC 97-19, page 307.

[29] AD Study Group, S. Maury (ed.), *The Antiproton Decelerator (AD)*, CERN/PS 99-50 (HP).

[30] E. J. N. Wilson (ed.), *Design Study of an Antiproton Collector for the Antiproton Accumulator (ACOL)*, CERN 83-10, page 25.

[31] M. Giovanozzi, J. Y. Hémery, C. Metzger, U. Mikkelsen, *Experimental Area of the CERN Antiproton Decelerator*, CERN/PS 98-47 (CA).

[32] http://psdoc.web.cern.ch/PSdoc/acc/ad/SelectMain/main.html

[33] AD Study Group, S. Maury (ed.), *Design Study of the Antiproton Decelerator: AD*, CERN/PS 96-43 (AR).

[34] S. Maury et al., *Commissioning and First Operation of the Antiproton Decelerator (AD)*, Proceedings from the 2001 Particle Accelerator Conference, Chicago, June18-22, 2001.

[35] S. P. Møller, *Cooling Techniques*, Proc. Fifth General Accelerator Physics Course, Vol. II, CERN 94-01, 601-618.

[36] D. Möhl, *Stochastic Cooling*, Proc. Fifth Advanced Accelerator Physics Course, Vol. II, CERN 95-06, 587-672.

[37] J. Bosser, *Electron Cooling*, Proc. Fifth Advanced Accelerator Physics Course, Vol. II, CERN 95-06, 673-730.

[38] M. Weiss, *Radio-Frequency Quadrupole*, Proc. Fifth Advanced Accelerator Physics Course, Vol. II, CERN 95-06, 959-992.

[39] A. M. Lombardi, *Accelerating and Decelerating RFQs*, Proc. Linear Accelerator Conference, Chicago 1998, 377-381.

[40] A. M. Lombardi, W. Pirkl, *First Operating Experience with the CERN Decelerating RFQ for Antiprotons*, Proc. Particle Accelerator Conference, Chicago, June 18-22, 2001.

[41] P. Tykesson, *Ionkilder*, Noter til kursus i eksperimentel teknik.

[42] http://www.isa.au.dk/elisa/elisa.html

[43] H. Knudsen, U. Mikkelsen, S. P. Møller, R. Thompson and E. Uggerhøj, *Construction of an Electrostatic Analyzer (ESA) for Energy Loss Measurements at the CERN AD*, CERN PS/CA Note 99-23.

[44] J. L. Wiza, *Microchannel Plate Detectors*, Nucl. Instrum. Methods, **162** (1979) 587.

[45] Hamamatsu Photonics, *Circular MCP and Assembly Series*, Technical Data No. T-114.

[46] Erik Lægsgaard, *Introduktion til detektorer*, Forelæsningsnoter, Aarhus Universitet, 1989.

[47] W. Weise, *Antinucleon - nucleon annihilation*, LEAP, Proc. 92, page 220c

[48] http://www.ni.com/labview/what.htm

[49] http://root.cern.ch

[50] P. E. Hodgson, E. Gadioli and E. Gadioli Erba, *Introductory Nuclear Physics*, Oxford Science Publication, 1997.

[51] N. R. Arista and A. F. Lifschitz, Nucl.Instrum. Methods. B (in press).

[52] R. Golser and D. Semrad, *Observation of a Striking Departure from Velocity Proportionality in Low-Energy Electronic Stopping*, Phys. Rev. Lett. **66** (1991) 1831.

[53] K. Eder, D. Semrad, P. Bauer, R. Golser, P. Maier-Komor, F. Aumayr, M. Peñalba, A. Arnau, J. M. Ugalde and P. M. Echenique, *Absence of a "Threshold Effect" in the Energy Loss of Slow Protons Traversing Large-Band-Gap Insulators*, Phys. Rev. Lett. **79** (1997) 4112.

[54] G. Konac, S. Kalbitzer, Ch. Klatt, D. Niemann and R. Stoll, *Energy Loss and Straggling of H and He Ions of keV Energies in Si and C*, Nucl. Instrum. Methods **B136-138** (1998) 159.

Dansk Resumé

Eksperimentelle undersøgelser af energitabet af langsomme protoner og antiprotoner i stof

Ladede partiklers bevægelse igennem stof har været studeret siden begyndelsen af det 20. århundrede. Niels Bohr var en af de første til at studere disse fænomener i detaljer først ved hjælp af klassisk mekanik, men senere også ved hjælp af kvantemekanik.

Når en ladet partikel bevæger sig igennem stof, vil den miste energi på grund af elektromagnetiske vekselvirkninger med stoffet. Energitabet per længdeenhed kaldes stoffets stoppeevne, og den er afhængig af projektilets ladning og hastighed samt stoppe-materialets sammensætning. Vekselvirkningerne kan deles op i to dele: Elastiske stød med stoffets atomer i helhed samt uelastiske stød med atomernes elektroner. De elastiske stød er to-legeme problemer, hvor impuls fra projektilet bliver overført til hele atomet, mens de uelastiske stød med elektronerne fører til ekscitation og ionisation af atomerne. På grund af elektronskyernes store rumlige udstrækning i forhold til atomkernerne vil den største bidrag til projektilets energitab komme fra vekselvirkning med elektronerne dvs. de uelastiske stød. Dermed vil energitabet være størst når der er resonans imellem projektilet og elektronerne det vil sige, når projektilets hastighed er af samme størrelse som elektronernes hastighed omkring atomkernen, fordi vekselvirkningen vil i så fald virke i "længst tid". Hvis projektilets hastighed er større, vil vekselvirkningstiden være kortere og impulsoverførslen mindre ($\Delta\mathbf{p} = \mathbf{F}\Delta t$), mens for lavere projektilhastigheder bliver vekselvirkningerne mere og mere adiabatiske, som også medfører nedsat energitab.

Et meget interessant fænomen i forbindelse med energitabet er Barkas effekten, som fører til mindre energitab af negative projektiler i forhold til positive projektiler. Dette skyldes polarisering af stoffets atomer, idet de negative projektiler vil frastøde stoffets elektroner mens de positive vil tiltrække dem, hvormed der vil være "mere elektronsky" at vekselvirke med for de positive projektiler end for de negative. Barkas effekten er størst når stødtiden er lang nok til at stoffets atomer kan indrette sig for den indkommende projektil, det vil sige ved lave

projektilhastigheder under energitabsmaksimum. Ved høje projektilhastigheder, svarende til kinetiske energier over 2-3 MeV, bliver Barkas effekten så lille, at den slet ikke kan måles.

For at studere Barkas effekten, har der været udført en række energitabs-målinger med antiprotoner ved lavenergi antiproton ringen på CERN i Geneve. Her er det lykkedes at komme helt ned til energier hvor energitabet opnår sit maksimum, og man har da også observeret, at energitabet for antiprotoner var omkring 35 % lavere end for protoner. Formålet med eksperimenterne beskrevet i denne afhandling var, at fortsætte målingerne endnu længere ned til projektilenergier langt under energitabsmaksimum, som er omkring 100 keV for de fleste stoffer. Her findes der ingen energitabsmålinger med antiprotoner.

Disse målinger er idag mulige ved den nye antiprotonfacilitet på CERN, Antiproton Deceleratoren (AD). AD'en er en erstatning for den tidligere antiproton-kompleks, som bestod af følgende maskiner: Proton Synkrotronen (PS), Antiproton Accumulator (AA), Antiproton Collector (AC) og Lav Energi Antiprton Ringen (LEAR). Antiptonerne bliver fremstillet med en impuls på omkring 3.57 GeV/c og nedbremset i AD ringen til 100 MeV/c, svarerende til en kinetisk energi på 5.3 MeV. Efter ekstraktion fra AD'en, bliver antiprotonerne nedbremset yderligerre ved hjælp af en *Radio Frekvens Kvadropol Decelerator* (RFQD) til en kinetisk energi, som kan varieres imellem 0 og 120 keV. Systemet kan levere omkring 10^7 antiprotoner hvert andet minut ved disse hidtil uhørt lave antiproton energier.

Til selve energitabsmålingerne er der blevet konstrueret et elektrostatisk spektrometer, som kunne måle projektilernes energi før og efter passage igennem targetmaterialet. Dette spektrometer havde den store fordel i forhold til tidligere energitabs-måleapparater, at man kunne sætte en positiv eller negativ højspænding på target, og dermed variere projektilenergien uden at skulle ændre på accelerator/decelerator indstillinger. På denne måde kunne man lave en hel måleserie fra 1 til 90 keV ved kun at ændre accelerator/decelerator indstillingerne en eller to gange. Spektrometer er blevet testet med protoner i energiområdet 1..40 keV ved at sammenligne resultaterne med eksisterende målinger.

I alt er det lykkedes at måle energitabet for fem materialer nemlig kulstof, aluminium, nikkel, guld og litiumfluorid og dermed dække et forholdsvis bredt område i atomnummer fra 6 til 79. Energiområdet for antiprotonmålingerne strækker sig fra 2 til 90 keV med varienrende aktuelle grænser for de enkelte materialer. Målingerne for aluminium, nikkel og guld er absolutte målinger, mens for kulstof og litiumfluorid var det kun muligt at opnå relative målinger, idet folietykkelsen kunne kun bestemmes ved at normalisere protonmålingerne til tidligere målinger.

Ud fra vores målinger har vi vist, at energitabet for antiprotoner (under 30 keV) i kulstof, aluminium, nikkel og guld falder proportionalt med deres hastighed. Dette er et meget vigtigt resultat, fordi den bekræfter gyldigheden af

de teorier som forudsiger et hastighedsproportionalt energitab i de lave energi-områder. Protonmålinger har man ikke kunnet bruge til dette, fordi protoner deltager i elektronindfangningsprocesser, som er meget svære at inkludere i teoretiske modeller. Man har da også observeret store afvigelser fra hastigheds-proportionalt energitab for protoner i ædelgasser.

For litiumfluorid kan vi ikke udtale os om energitabets hastighedsproportion-alitet på grund af for stor spredning i vores målinger. En forsigtig skøn tyder dog på en lidt mere stejl afhængighed end hastighedsproportional.

Vi har naturligvis også målt Barkas effekten for de nævnte folier. Her har vi fundet, at energitabet for antiprotoner er reduceret med 40% til 55% ved 10 keV i forhold til energitabet for protoner ved den tilsvarende energi.

Antiprotonmålingerne er også blevet sammelignet med beregninger fra forskellige teoretiske modeller. Her har vi fundet, at den nye *Binære Teori* af Peter Sigmund og Andreas Schinner giver en god, såvel kvalitativ som kvantitativ, beskrivelse af antiprotonernes energitab. Allan Sørensens elektrongas model for meget lave energier giver også forudsigelser, som er i god overenstemmelse med de fleste af vores målinger.

Derudover har vi for protoner kunnet bestemme energitabsspredningen (strag-gling), som kommer fra stødprocessernes stokastiske natur. Disse spredninger har vi sammelignet med forudsigelserne af en elektrongas model af Wang og Ma og fundet pæn overensstemmelse for aluminium, nikkel og guld, men ikke for kulstof.

Med hensyn til fremtidige eksperimenter er det vigtigt at få mere nøjagtige målinger for isolatorer som litiumfluorid. Litiumfluorid har et stort båndgab på 14 eV, som er sammenlignelig med ædelgassernes laveste excitationsenergier. Dermed vil man også forvente en afvigelse fra hastighedsproportional energitab for stort-båndgab-isolatorer, som man har observeret for nogle ædelgasser. Med protoner har man ikke kunnet observere sådanne afvigelser, og man har forklaret det med eksistensen af en bundet tilstand imellem den positive projektil (protonen) og en elektron i materialet, hvilket fører til en lokal reduktion af båndgabet. Denne bundne tilstand eksisterer imidlertid ikke for antiprotoner, hvormed afvigelse fra hastighedsproportionalt energitab stadig kan forventes.

Det er vigtigt at have både kvalitativ og kvantitativ viden om ladede partiklers energitab igennem stof. Foruden de akademiske værdier har den mange anven-delsesmuligheder indenfor f.eks. strålebehandling, halvlederindustri og rumfart.